



HAL
open science

X3: A High-mass Young Stellar Object Close to the Supermassive Black Hole Sgr A

Florian Peißker, Michal Zajaček, Nadeen B. Sabha, Masato Tsuboi, Jihane Moultaqa, Lucas Labadie, Andreas Eckart, Vladimír Karas, Lukas Steiniger, Matthias Subroweit, et al.

► **To cite this version:**

Florian Peißker, Michal Zajaček, Nadeen B. Sabha, Masato Tsuboi, Jihane Moultaqa, et al.. X3: A High-mass Young Stellar Object Close to the Supermassive Black Hole Sgr A. *The Astrophysical Journal*, 2023, 944, 10.3847/1538-4357/aca977 . insu-04198463

HAL Id: insu-04198463

<https://insu.hal.science/insu-04198463>

Submitted on 7 Sep 2023

HAL is a multi-disciplinary open access archive for the deposit and dissemination of scientific research documents, whether they are published or not. The documents may come from teaching and research institutions in France or abroad, or from public or private research centers.

L'archive ouverte pluridisciplinaire **HAL**, est destinée au dépôt et à la diffusion de documents scientifiques de niveau recherche, publiés ou non, émanant des établissements d'enseignement et de recherche français ou étrangers, des laboratoires publics ou privés.



Distributed under a Creative Commons Attribution 4.0 International License



X3: A High-mass Young Stellar Object Close to the Supermassive Black Hole Sgr A*

Florian Peißker¹, Michal Zajaček², Nadeen B. Sabha³, Masato Tsuboi⁴, Jihane Moutaka⁵, Lucas Labadie¹, Andreas Eckart^{1,6}, Vladimír Karas⁷, Lukas Steiniger¹, Matthias Subroweit¹, Anjana Suresh¹, Maria Melamed¹, and Yann Clénet⁸

¹ I.Physikalisches Institut der Universität zu Köln, Zùlpicher Str. 77, D-50937 Köln, Germany; peissker@ph1.uni-koeln.de

² Department of Theoretical Physics and Astrophysics, Faculty of Science, Masaryk University, Kotlářská 2, 611 37 Brno, Czech Republic

³ Institut für Astro- und Teilchenphysik, Universität Innsbruck, Technikerstr. 25, A-6020 Innsbruck, Austria

⁴ Institute of Space and Astronautical Science, Japan Aerospace Exploration Agency, 3-1-1 Yoshinodai, Chuo-ku, Sagami-hara, Kanagawa 252-5210, Japan

⁵ Institut de Recherche en Astrophysique et Planetologie (IRAP), Université de Toulouse, CNRS, Observatoire Midi-Pyrénées (OMP), Toulouse, France

⁶ Max-Planck-Institut für Radioastronomie, Auf dem Hügel 69, D-53121 Bonn, Germany

⁷ Astronomical Institute, Czech Academy of Sciences, Boční II 1401, CZ-14100 Prague, Czech Republic

⁸ LESIA, Observatoire de Paris, Université PSL, CNRS, Sorbonne Université, Université de Paris, 5 place Jules Janssen, F-92195 Meudon, France

Received 2022 November 10; revised 2022 December 4; accepted 2022 December 5; published 2023 February 28

Abstract

To date, the proposed observation of young stellar objects (YSOs) in the Galactic center still raises the question of where and how these objects could have formed due to the violent vicinity of Sgr A*. Here, we report the multiwavelength detection of a highly dynamic YSO close to Sgr A* that might be a member of the IRS 13 cluster. We observe the beforehand known coreless bow-shock source X3 in the near- and mid-infrared (NIR/MIR) with SINFONI (VLT), NACO (VLT), ISAAC (VLT), VISIR (VLT), SHARP (NTT), and NIRCAM2 (KECK). In the radio domain, we use CO continuum and H30 α ALMA observations to identify system components at different temperatures and locations concerning the central stellar source. It is suggested that these radio/submillimeter observations in combination with the NIR Br γ line can be associated with a protoplanetary disk of the YSO, which is consistent with manifold VISIR observations that reveal complex molecules and elements such as PAH, S IV, Ne II, and Ar III in a dense and compact region. Based on the photometric multiwavelength analysis, we infer the mass of $15_{-5}^{+10} M_{\odot}$ for the YSO with a related age of a few 10^4 yr. Due to this age estimate and the required relaxation timescales for high-mass stars, this finding is an indication of ongoing star formation in the inner parsec. The proper motion and 3D distance imply a relation between X3 and IRS 13. We argue that IRS 13 may serve as a birthplace for young stars that are ejected due to the evaporation of the cluster.


Unified Astronomy Thesaurus concepts: Galactic center (565); Young stellar objects (1834); Massive stars (732); Star formation (1569); Young massive clusters (2049); Stellar bow shocks (1586); Supermassive black holes (1663)

Supporting material: animations

1. Introduction

The properties of star formation are well defined and require environments characterized by a sufficiently low temperature (<20 K) and a high gas density (Hsieh et al. 2021). In contrast, the temperature of gaseous-dusty filaments in the Galactic center (GC) exceeds a gas temperature of ~ 6000 K and a dust temperature of ~ 250 K (Cotera et al. 1999; Moser et al. 2017). Furthermore, the velocity dispersion of all known objects close to Sgr A* outpaces typical numerical values in star formation regions by several magnitudes (Larson 1981; Genzel et al. 2000). Due to the presence of the $4 \times 10^6 M_{\odot}$ supermassive black hole Sgr A*, tidal forces hinder gas clumping, which is necessary for the formation of stars. However, Yusef-Zadeh et al. (2013) found, at a distance of about 0.6 pc from Sgr A*, SiO clumps that imply high-mass star formation. The authors suggest that the observed clumps are an indication of in situ star formation that took place during the last 10^4 – 10^5 yr. In a subsequent analysis, ALMA observations showed high-velocity clumps in the inner parsec but also within the

circumnuclear disk (CND) directed toward Sgr A* (Moser et al. 2017; Hsieh et al. 2021). Some of these dense clumps meet the conditions necessary for star formation. In addition, Jalali et al. (2014) propose that the interplay between Sgr A* and inspiraling clumps of several 10 solar masses could trigger star formation. Similar interpretations of the observational findings can be found in the theoretical works of Nayakshin et al. (2007) and Hobbs & Nayakshin (2009). The inspiraling of clumps and/or clusters was already suggested by Portegies Zwart et al. (2003) and Maillard et al. (2004) to explain the high-mass stars of IRS 13 and IRS 16 (for a review, see Genzel et al. 2010). While the IRS 16 cluster is the origin of prominent stellar winds originating at high-mass stars (Krabbe et al. 1991, 1995), IRS 13 could contain dust-enshrouded young stellar objects (YSOs) (Eckart et al. 2004) and evolved Wolf-Rayet (WR) stars (Moutaka et al. 2005). The presence of dusty objects of IRS 13 are accompanied by the finding of dusty D-sources in or close to the S-cluster (Eckart et al. 2013; Peißker et al. 2020b).⁹ It is evident that the finding of two distinct populations with sources that share photometric properties such as the $H-K$ and $K-L$ colors imply a common formation history. Furthermore, it is suggested that

 Original content from this work may be used under the terms of the [Creative Commons Attribution 4.0 licence](https://creativecommons.org/licenses/by/4.0/). Any further distribution of this work must maintain attribution to the author(s) and the title of the work, journal citation and DOI.

⁹ Ciurlo et al. (2020) denote these objects as G-sources.

Table 1
Telescopes and Instruments Used in This Work

Telescope/Instrument	Wavelength (μm)
VLT(NACO)	1.6, 2.1, 3.8, 4.7
VLT(SINFONI)	1.4–2.3
VLT(ISAAC)	3.0–4.5
VLT(VISIR)	8.0–20.0
NTT(SHARP)	2.2
NIRCAM2(KECK)	1.6, 2.1, 3.7
OSIRIS(KECK)	2.1
ALMA	874, 1292

Note. The listed wavelength for the ALMA observations corresponds to 232 and 343 GHz.

more sources such as X7 (Peißker et al. 2021a) and G2/DSO (Peißker et al. 2021c) can be found in the inner parsec (Yusef-Zadeh et al. 2015, 2017).

The previously identified bow-shock source X3, which was assumed to be coreless, is located at a distance of about $1''$ from IRS 13 (Clénet et al. 2003; Mužić et al. 2010). It is speculated that the bow-shock shape of X3 is created by stellar winds originating at the IRS 16 cluster (Wardle & Yusef-Zadeh 1992; Peißker et al. 2021a). Here we revisit the morphological and emission properties of the bow-shock source X3 by analyzing an extensive archival data set observed between 1995 and 2020. The near- and mid-infrared (NIR/MIR) observations were carried out in the H ($1.65 \mu\text{m}$), K ($2.20 \mu\text{m}$), L ($3.80 \mu\text{m}$), and M bands ($4.80 \mu\text{m}$) with a total on-source integration time of several weeks. The MIR domain is accompanied by narrow-filter observations between 8 and $20 \mu\text{m}$ using VISIR covering the N and Q bands. In addition to radio/submillimeter observations at 232 GHz ($1292 \mu\text{m}$) and 343 GHz ($874 \mu\text{m}$), we include three-dimensional Integral Field Unit (IFU) data cubes observed with SINFONI. Based on the analysis presented here, we propose the detection of a high-mass YSO (HMYSO) associated with X3 characterized by strong outflows with velocities of several hundred km s^{-1} . This surprising and novel interpretation of the X3 system suggests an urgent need to revise our view on this one and similar objects in the Milky Way center. To justify our claim, we will investigate the spectral footprint of the X3 system and compare it to close-by early- and late-type stars. Furthermore, we present a comprehensive multiwavelength analysis to target the complexity of the X3 system. We discuss formation scenarios consistent with theoretical models that aim to explain the origin of young stars in the inner parsec.

In the following Section 2, we provide an overview of the different telescopes, instruments, and methods that are used for the analysis. Hereafter, we present the main results in Section 3. These results will be discussed in Section 4 and are followed by the conclusions in Section 5.

2. Data and Tools

In this section, we describe the data and analysis tools that are used in this work. Data tables can be found in Appendix A. In Table 1, we list all the instruments/telescopes used with the corresponding wavelength domain. Throughout this work, we will not distinguish between the various subbands such as, for example, the K_S , K' , and K bands since the color difference ($|K-K'|$, $|K-K_S|$, $|K'-K_S|$) is smaller than the typical photometric uncertainty of about 0.1–0.2 mag (Ott et al. 1999; Eckart et al. 2004).

2.1. Very Large Telescope

The Very Large Telescope (VLT) is located at Cerro de Paranal (Chile) at a height of about 2500 m. The VLT harbors four main telescopes (unit telescopes, abbreviated with UTs) with an individual dish size of 8.2 m and four smaller auxiliary telescopes (ATs) with a dish size of 1.8 m each. While every UT is capable of adaptive optics (AO) to correct for the turbulent atmosphere using a natural guidance star (NGS), UT4 additionally supports the use of a laser guide star (LGS). Except for VISIR, the VLT instruments SINFONI, NACO, and ISAAC are already decommissioned. However, ERS (Davies et al. 2018) is the successor to NACO and SINFONI, which combines the capabilities of both instruments.

2.1.1. SINFONI and NACO

SINFONI (Eisenhauer et al. 2003; Bonnet et al. 2004) is an NIR instrument that operates between 1.1 and $2.45 \mu\text{m}$ and is supported by an IFU. The IFU is responsible for the shape of the data, which are arranged as a 3D cube containing two spatial and one spectral dimension. This data setup allows for the analysis of individual emission lines by subtracting the underlying continuum. If the source of interest exhibits a line-of-sight (LOS) velocity with $\neq 0 \text{ km s}^{-1}$, it is identical to the Doppler shift of a line with respect to the rest wavelength. Since the K band around $2.2 \mu\text{m}$ is not affected by telluric emission and absorption features, the $\text{Br}\gamma$ line with a rest wavelength of $2.1661 \mu\text{m}$ is commonly used for the analysis of stars in the K band because of the minimized confusion.

For the observations, an exposure time of 300 s per single data cube is used. By combining and stacking single data cubes, we are able to artificially increase the on-source integrating time. The spatial pixel scale for the here presented SINFONI data is $0''.1$ with a field of view (FOV) of $3'' \times 3''$ per single data cube; the grating is set to the $H+K$ band ($1.45\text{--}2.45 \mu\text{m}$) with a spectral resolution $R = \frac{\lambda}{\Delta\lambda} = 1500$. With a central wavelength in the $H+K$ band of $\lambda = 1.95 \mu\text{m}$, we get the value for the smallest distinguishable wavelength of $\Delta\lambda = 0.0013 \mu\text{m}$. This, however, is an upper limit since the point-spread function (PSF) and therefore the computed spectral resolution differ as a function of position on the detector.¹⁰ Using the measured values from the instrument commissioning, we adapt the line uncertainty of $\pm 25 \text{ km s}^{-1}$.

In addition to SINFONI, we use the NIR imager NACO (Lenzen et al. 2003; Rousset et al. 2003) in the H , K , L , and M bands with an FOV of about $15'' \times 15'' \approx 0.6 \text{ pc} \times 0.6 \text{ pc}$ that shows almost the entire NSC/inner parsec of the GC. Because of the size of the FOV, the bright supergiant IRS 7 is regularly used for AO. We choose the standard randomized dither pattern inside the largest dither box of $4''$. Calibration data like sky, flat, and dark frames are observed with a standard procedure and are provided by the telescope site.¹¹ The reduction of the data is done by using DPUSER (Ott, MPE Garching) as well as in-built scripts such as dead pixel correction.

2.1.2. ISAAC and VISIR

The Infrared Spectrometer And Array Camera (ISAAC; see Moorwood et al. 1998) and VLT Imager and Spectrometer for mid-Infrared (VISIR; see Lagage et al. 2004) instruments are

¹⁰ See the SINFONI manual, available at www.eso.org.

¹¹ Sky frames are obtained from a nearby empty region.

capable of performing imaging and spectroscopic observations in the MIR domain. The ISAAC data, which are used to create an MIR cube (3.0–4.5 μm), are already discussed and analyzed in Moultaqa et al. (2005), where the authors describe the reduction process in detail. The ISAAC observations were performed in 2003 July using the long-wavelength and low-resolution mode with $R=700$. In this list, VISIR is the only instrument that is currently mounted at the VLT, namely UT3. It is, like ISAAC, an MIR imager with spectrometer capabilities. In contrast to the continuum observations with ISAAC, several filters of VISIR were used. The selected filters for the observations that took place in 2004 are PAH1r1 (8.19 μm), PAH1 (8.59 μm), Ar III (8.99 μm), SIVr1 (10.02 μm), SIVr2 (11.11 μm), PAH2 (11.25 μm), NeIIr1 (12.51 μm), Ne II (12.81 μm), NeIIr2 (13.04 μm), Q2 (18.72 μm), and Q3 (19.50 μm). In order to increase the signal-to-noise ratio, we stack individual frames to create a final mosaic.

2.2. NTT Telescope

The ESO New Technology Telescope (NTT) uses active optics to correct for distortion effects caused by the dish (~ 3.6 m). It was commissioned in 1989 and hosted instruments such as the NIR Speckle-Camera SHARP. The data used in the work was published in Menten et al. (1997) and is high-pass-filtered with the Lucy–Richardson algorithm (Lucy 1974). We refer to Peißker et al. (2020a, 2022) where we describe and discuss different aspects of the high-pass-filter technique.

2.3. Keck Observatory

The Keck observatory is located at Mount Maunakea. With an elevation of over 4000 m, it is one of the highest ground-based observatories. The observatory consists of two single telescopes, Keck I and Keck II with a dish size of 10 m each. Both telescopes can work as an interferometer with an increased baseline compared to the single-dish setup.

2.3.1. NIRCAM2

NIRCAM operates in the NIR in the K_S band at a central wavelength of 2.12 μm . The spatial pixel scale is 0.0099 mas, and the size of a single exposure with an FOV of about $10'' \times 10''$ is comparable to the NACO data. We use the KOA archive¹² to download data observed in 2019. For the observations carried out in 2019 (PI: Tuan Do, UCLA), an LGS was used to perform the AO correction. We use the precalibrated, i.e., science-ready, data (dark-, flat-, and sky-corrected) and apply the shift and add the algorithm to maximize the signal-to-noise ratio.

2.3.2. OSIRIS

The OH-Suppressing Infrared Imaging Spectrograph (OSIRIS) mounted at the Keck II telescope. Like SINFONI, OSIRIS provides 3D data cubes that consist of two spatial and one spectral dimension (Larkin et al. 2006; Mieda et al. 2014) and uses an integrated field spectrograph (IFS) supported by an AO. For the purpose of guidance in a crowded FOV, a science camera is coupled with the instrument producing the NIR continuum data. For this work, we will utilize this science camera and investigate the K -band emission of the X3 system in 2020. The presented data

were observed with the Kn3 filter that represents the K band (2.12–2.22 μm). The corresponding FOV is 2048×2048 pixels and has a spatial resolution of 10 mas. The science-ready archival data downloaded from the Keck Online Archive (KOA) is shifted and added to suppress noise and artifacts.

2.4. ALMA

The Atacama Large (Sub)Millimeter Array (ALMA) is located on the Chajnantor plateau. With 66 radio telescopes with a maximum distance of about 16 km between single units, it is the largest ground-based observatory to date. The antennas cover a wavelength range of 31–1000 GHz. Here used data (PI Masato Tsuboi, project code: 2015.1.01080.S) was previously discussed and analyzed in Tsuboi et al. (2017, 2019, 2020a, 2020b) and makes use of Band 7 (≈ 350 GHz). In addition, we use archival science-ready data¹³ observed at 232 GHz ($H_{30\alpha}$) by PI Lena Murchikova (project code: 2016.1.00870.S, see Murchikova et al. 2019).

2.5. Methods

In the following, we will describe the analyzing techniques used in this work. Since we used and discussed these tools in detail in previous works (e.g., Peißker et al. 2020a, 2020b), we will refer the reader to the related publications.

2.5.1. High-pass Filter

For the K -band detection presented in Figure 1, we used a high-pass filter to minimize the influence of overlapping PSF. We applied the high-pass filter that can be described as an image sharpener to all H - and K -band images presented in this work (except the $\text{Br}\gamma$ line maps shown in Figures 8 and 23, Appendix D). The motivation for this process is the extended PSF wings of bright sources in the investigated FOV. If the PSF and especially its wings become too dominant, some image details are suppressed. The process is outlined in the following:

1. The input image (I_{in}) is smoothed with a Gaussian that matches the PSF of I_{in} .
2. The resulting image I_{low} is a low-pass-filtered version of I_{in} .
3. I_{in} is the result of the real image (i.e., the natural scene without the influence of a PSF) composed with an “all-filter” PSF.

This above relation can be mathematically described with

$$I_{\text{in}} - I_{\text{low}} = I_{\text{high}}, \quad (1)$$

where I_{high} is the desired high-pass-filtered image of the input frame. In addition to the process described, we can again use a Gaussian and apply it to I_{high} to construct a smoothed version of the final result. With this procedure, broader PSF wings are again added to the data. However, the influence of the PSF wings is significantly reduced. In Peißker et al.’s (2022) Figure 2, we show a comparison between filtered and nonfiltered data to visualize the advantage of an image sharpener. Compared to the Lucy–Richardson algorithm (Lucy 1974), the *image sharpener* is accessible and easy to use. It can be classified as a cosmetic procedure and shows similarities to angular

¹² <https://koa.ipac.caltech.edu/cgi-bin/KOA/nph-KOAlugin>

¹³ <https://almascience.eso.org/aq/>

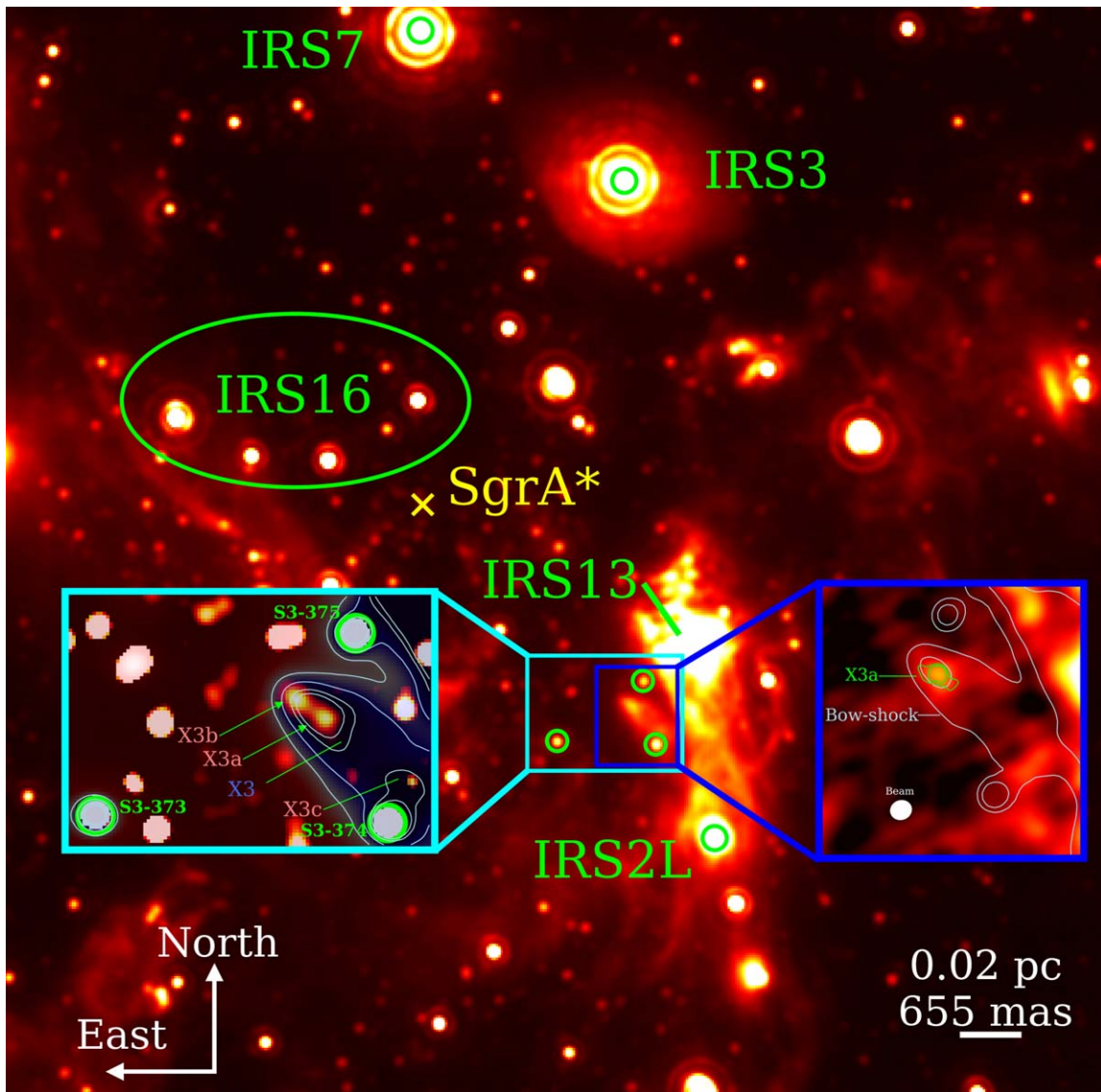


Figure 1. Finding chart for the X3 system. We show two zoomed views toward the X3 system. The cyan zoom box to the left shows a K - and L -band overlay image where blue represents the dust of the bow shock and red is associated with hot and thermal emission. Whereas X3a can be classified as a YSO, X3b and X3c are thermal blobs. The cyan box also indicates the position of the three closest and brightest stars, S3-373, S3-374, and S3-375 (see Gautam et al. 2019). The blue box on the right shows the CO emission at 343 GHz where we incorporate K -band contours of X3a (lime colored) and the bow shock, which is primarily observed in the L band (light-blue colored). The background image is observed with NACO in the MIR (L band, $3.8 \mu\text{m}$), where we indicate prominent clusters like IRS 16 or IRS 13 and stars. Sgr A* is located at the position of the yellow \times .

differential imaging (Marois et al. 2006). However, we add that the SHARP data of 1995 (see Section 3 and Menten et al. 1997) are treated with a Lucy–Richardson (LR) deconvolution algorithm. We guide the interested reader to Peißker et al. (2022) for a detailed description of the LR process.

2.5.2. Keplerian Fit

For the trajectory of X3, Mužić et al. (2010) derived a linear solution. Since we have access to a data baseline that is twice as long as the one analyzed by Mužić et al. (2010), we will apply a Keplerian solution to the data. Based on the analysis in Parsa et al. (2017), Ali et al. (2020), and Peißker et al. (2022), we assume a mass of $4.0 \times 10^6 M_{\odot}$ with a distance of 8.0 kpc for the central potential Sgr A*. This assumption is justified by the independently derived mass of $4.0 \times 10^6 M_{\odot}$ for Sgr A* by

Akiyama et al. (2022) and in reasonable agreement with Do et al. (2019).

2.6. Theoretical Models

To put the observational photometric results into perspective, we apply the 3D radiative transfer MCMC model by Robitaille (2011) to model the spectral energy distribution (SED) for the X3 system. The code called HYPERION is based on a 3D dust continuum emission model where ray tracing is used to enhance the results. A detailed documentation of the code is freely accessible.¹⁴ HYPERION takes various structures of YSOs into account. For example, the gaseous accretion disk, bipolar cavities, and a rotationally flattened infalling dust

¹⁴ www.hyperion-rt.org

Table 2
Components of the X3 System

Name	Classification
X3	Bow-shock dust envelope
X3a	Central stellar source
X3b	Hot thermal blob
X3c	Hot blob?

Note. While we find strong evidence in our data set that justifies the listed classification of X3, X3a, and X3b, the analysis of X3c remains challenging.

envelope (Ulrich type; see Ulrich 1976) can be modeled. We refer the interested reader to the publication of Sicilia-Aguilar et al. (2016) where the authors provide a rough overview of the composition of a YSO (see Section 4). An additional example of successful application of the code can be found in Zajaček et al. (2017), where we successfully modeled the NIR continuum emission of the excess-infrared source DSO/G2 using similar gaseous-dusty structures typical of YSOs as for the X3 system. For the dust grains, we use a model that is supposed to represent the dust envelope of the X3 system. Our dust model is based on Draine (2003) with a slope of the optical extinction curve of $R_V = A_V / (A_B - A_V) = 3.1$, which appears to be suitable and agrees with detailed high-resolution studies of the region by Fritz et al. (2011).

3. Results

In this section, we present the results of our multiwavelength analysis. In the following section, we analyze the data that reveal the stellar counterpart of X3 with its components that are related to a YSO. Based on the presented observations and the SED model, we derive various parameters that describe the young dust-enshrouded star. In Figure 1, we provide an overview of the components that are associated with the X3 system. The three brightest and closest early-type stars to X3 are arranged as a triangle, which is used throughout this article for guidance to identify the investigated system in the crowded field. Please note that we adopt the nomenclature of Gautam et al. (2019) for S3-374. Since the other two stars of the triangle are not named yet, we are following the established nomenclature with S3-373 and S3-375. The cyan box in Figure 1 shows the three triangle stars S3-373, S3-374, and S3-375. In the following, all figures are normalized to their peak flux intensity to maintain a comparable character. Some of the closer stars might be oversaturated due to the intrinsic flux density of X3.

3.1. Near- and Mid-infrared Detection

During the analysis of NACO data observed in 2004, we found at the position of the dusty L -band bow-shock source X3 three compact sources, which we call X3a, X3b, and X3c (see Figure 1 and Table 2 for an overview). K -band observations with the SHARP camera (NTT) of 1995 (see Figure 2 in Menten et al. 1997) in comparison with the NACO (VLT) data of 2002 imply the absence of X3b in earlier years while X3a can be detected well above the confusion limit between 1995 and 2020. Setting X3a as a reference source, we find that the distance of X3b decreases between 2002 and 2011 (see the K -band observations in Appendix B, Figure 20). In the years following 2011, the data do not show any significant K -band flux above the noise level for X3b. This is unexpected

especially because the magnitude of X3b was higher compared to X3a in 2002. We pick three epochs to reflect this dynamical behavior of the X3 system. From the data, it is apparent that X3b exhibits no K -band emission above the noise level at the expected position either in 1995 or 2019 (Figure 2).

In addition to X3b, we observed a second blob in the L band that moves along with X3a between 2002 and 2019. To exclude the chance of a sporadic flyby, we center the available L -band NACO data on the position of the dusty envelope X3. The resulting stacked data are shown in Figure 3 where we also indicate the position of X3c with respect to the bow shock X3 (see also Figure 1). We find a compact emission with an FWHM of about $0''.1$. If X3 and X3c are not related, the flux of the blob would have been canceled out as it is imminent from the low background emission displayed in Figure 3. In Section 4, we estimate the statistical probability for a random flyby event for objects close to the IRS 13 cluster based on the K -band luminosity function (KLF) formulated by Paumard et al. (2006).

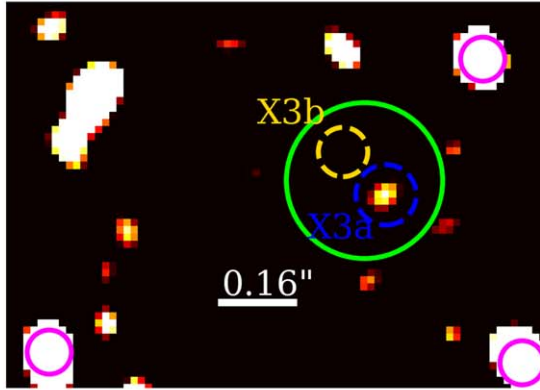
Furthermore, we determine the distance of X3 and X3a to Sgr A* using the orbital elements of the well-observed S2 orbit (Peißker et al. 2022). From the orbital fit of S2, we calculate the position of Sgr A*, which then is used as a reference position to derive the distance of X3 and X3a. To account for uncertainties caused by the detector (Plewa et al. 2018), we chose ± 0.5 pixel to additionally incorporate the footprint of the variable background as well as the large distance (> 0.1 pc) between the X3 system and Sgr A*. With the spatial pixel scale of NACO of $0''.0133$ (H and K bands) and $0''.027$ (L band), this translates to an uncertainty of ± 6.6 mas and ± 13.5 mas. A short clip showing X3 and X3c is appended. For the dust envelope X3 and the blob X3a, we find an averaged proper motion of 244 ± 27 km s $^{-1}$, as shown in Figure 4. Individual numerical values are 220 ± 30 km s $^{-1}$ for X3a (K band) and 229 ± 30 km s $^{-1}$ for the bow shock X3 (L band). For the H -band detection of X3a, we find a proper motion of 282 ± 30 km s $^{-1}$, which is slightly higher than that of the L and K bands. Given the lower data baseline and the higher noise level of the H -band data, this is expected. However, the estimation of the proper motion of X3 and X3a in the H , K , and L bands are in reasonable agreement considering the uncertainties of the analysis. The continuum data used for the proper motion observed with NACO are shown in Appendix B, Figures 19–21.

As mentioned above, the distance between X3a and X3b decreases between 2002 and 2012. In addition, we find a constant distance between X3a and X3c. We reflect this manifold behavior of the two components in Figure 5 where we assumed that X3b was created around 1995. However, any other assumed epoch for the creation of X3b before 2002 does not impact the overall trend of the decreasing distance between 2002 and 2011. From the data displayed in Figures 3 and 5, it is evident that the proper motion of X3c matches the estimated 244 ± 27 km s $^{-1}$ for X3a and the bow shock X3. Consequently, we identify without confusion all three components at their expected positions in 2019 (Figure 6).

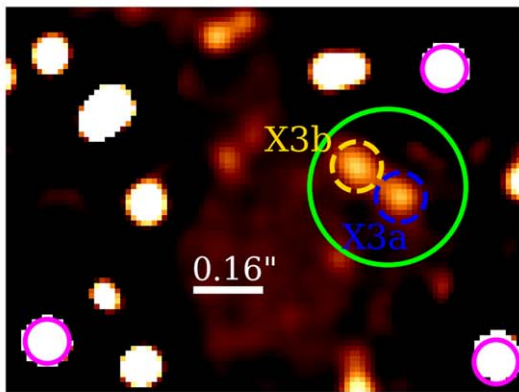
3.2. Line Emission of the X3 System

Inspecting SINFONI data observed in 2014 for spectroscopic analysis, we find several emission lines, such as Br10, Br δ , Br γ , He I, Pa γ , and the prominent [Fe III] multiplet related to

SHARP (K-band), 1995



NACO (K-band), 2002



NIRCAM2 (K-band), 2019

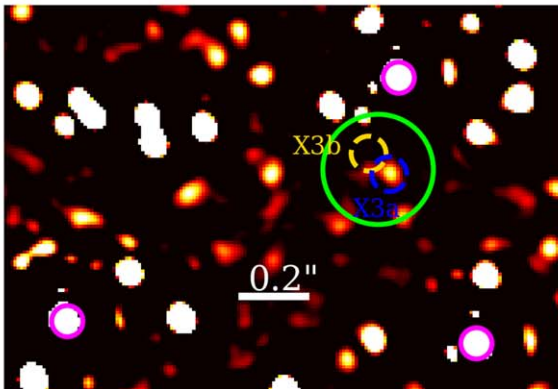


Figure 2. *K*-band detection of X3a in 1995, 2002, and 2019. The position of the dashed gold-colored circle marks the (expected) position of X3b. Because of the higher *K*-band magnitude of X3b compared to X3a in 2002, the blob should be traceable in 1995 and 2019. We indicate the position of X3a with a blue-colored dashed circle. For guidance, we marked the triangle stars S3-373, S3-374, and S3-375 with a magenta-colored circle (please see Figure 1). North is up, East is to the left.

X3a (see Figure 7). For the telluric-corrected¹⁵ SINFONI spectrum, we applied a 3 pixel aperture to the position of X3a. To avoid the contamination of the spectrum, we do not apply a background subtraction (see Appendix E for further discussion). The observed Br γ line exhibits a double-peak profile with a blue- and a redshifted velocity of -152 km s^{-1} and $+55$

¹⁵ We use the standard star Hip0 94122 for the telluric correction.

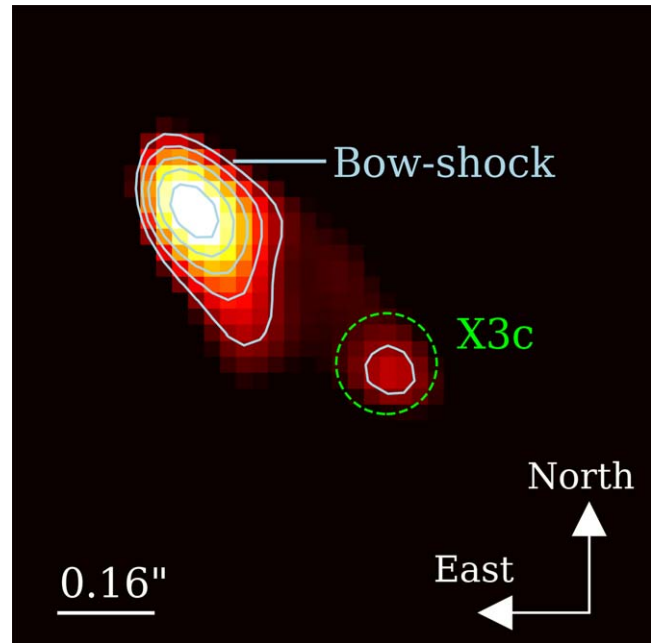


Figure 3. Dust blob X3c of the X3 system observed in the *L*-band with NACO. For the data presented, we stack all *L*-band NACO observations between 2002 and 2018 and subtract the triangle stars to emphasize the components of the system. We mark the position of X3 and the X3c blob. The contour lines refer to 20%, 40%, 60%, 80%, and 100% of the peak emission of the bow shock. Between 2002 and 2018, the distance of X3 to X3c stays constant. The measured projected length from tip to tail is about $0''.8$. An animation of this figure is available. The animation is of single years with stellar contributions from 2002 to 2018 and shows the correlation between X3 and X3c. The animation repeats the sequence but with a green circle to highlight X3c. The real-time duration of the animation is 12 s.

(An animation of this figure is available.)

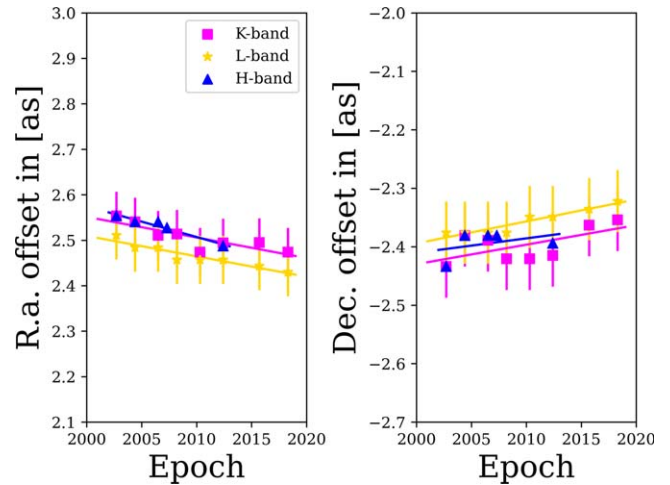


Figure 4. Proper motion of the X3 system based on NACO *H*-, *K*-, and *L*-band data. We use Sgr A* as the reference position. We derive an average proper motion of the X3 system of $244 \pm 27 \text{ km s}^{-1}$, where the uncertainty is the standard deviation. Because the fitted central position of the bow shock deviates due to its dimensions from the *K* and *H* bands, a certain offset is expected. However, the direction of the proper motion of all three objects is consistent, which is reflected by the fit.

km s^{-1} , respectively. The isolation of the Doppler-shifted Br γ lines and the subtraction of the underlying continuum reveal a compact gas emission at the position of X3a, which is shown in Figure 8. By selecting the individual Br γ peaks, we create two related line maps that show the distribution of the ionized gas.

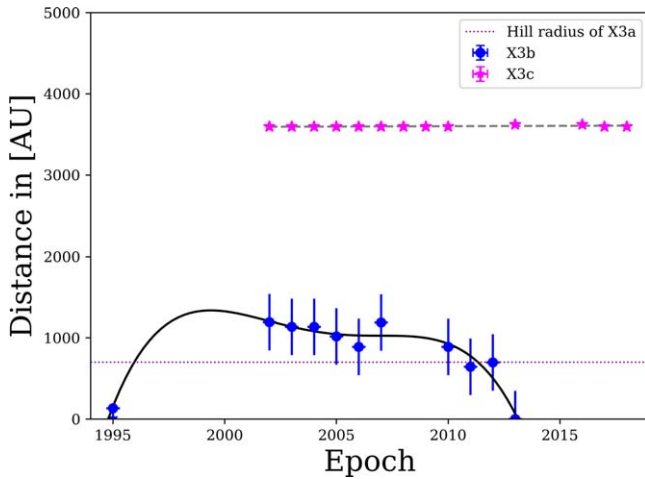


Figure 5. Distance of X3b and X3c with respect to X3a. We trace X3b without confusion until 2012 in the NACO *K*-band data (see Figure 20). The data implies that the thermal blob X3b got created or ejected between 1995 and 2002. Between 2002 and 2007, the distance of X3b to X3a stayed constant at about 1000 au. After 2012, we do not find any significant *K*-band emission above the detection limit at the expected position of X3b. In addition, we trace X3c without confusion along with X3 in the *L* band between 2002 and 2019. All data points show the related standard deviation of the fit (black and gray dashed line). The purple dotted line indicates the Hill radius where objects are expected to be significantly influenced by the gravitational field of X3a (see Section 4).

We append a short movie that shows the offset of the line, which we interpret as photoionized outflows originating in a gaseous disk close to X3a. Furthermore, we construct a position–position–velocity (PPV) map based on the Doppler-shifted $\text{Br}\gamma$ emission and include it in Figure 8. This PPV map shows a continuous velocity gradient with $\Delta v \approx 200 \text{ km s}^{-1}$. Analyzing the SINFONI spectrum, we find no tracers of CO band heads at 2.29, 2.32, 2.35, and 2.38 μm , implying a young age of X3a. The dimensions of the $\text{Br}\gamma$ -line distribution can be treated as an upper limit due to uncertainties imposed by the variable background and the marginally resolved emission.

Furthermore, we find a P Cygni profile for the NIR He I line observed with a blueshifted velocity of about -480 km s^{-1} (Figure 9), which indicates a stellar outflow of $\sim 400 \text{ km s}^{-1}$ when corrected for the LOS velocity of the source, which is $\sim -50 \text{ km s}^{-1}$ as inferred from the average of red and blue peaks of $\text{Br}\gamma$ line. Interestingly, the blueshifted $\text{Br}\delta$ velocity of -478 km s^{-1} matches the peak velocity of the P Cygni profile, implying a correlation and the potential origin of the recombination line in the outflow. A detailed investigation of a possible connection between $\text{Br}\delta$ and the P Cygni profile is beyond the scope of this work and should be analyzed separately. We note that Mizumoto et al. (2018) find [Fe II] emission lines related to the investigated P Cygni absorption profiles. From this work, it is plausible that emission and absorption features in the spectrum seem to be related. Table 3 lists all detected Doppler-shifted NIR emission lines as observed with SINFONI. In addition to the *H+K* band, we investigate the observation campaign that covers the region around X3, which was carried out with VISIR in the *N* and *Q* bands. Based on these MIR observations, we trace the Ne II, PAH1, Ar III, SIVr1, SIVr2, PAH2, Q2, and Q3 lines, which are associated with YSOs (Woitke et al. 2018). In Figure 10, we present a SIVr2 continuum map with the indicated position of X3. All other lines are shown in Appendix B, Figure 22. Although the spatial pixel scale of

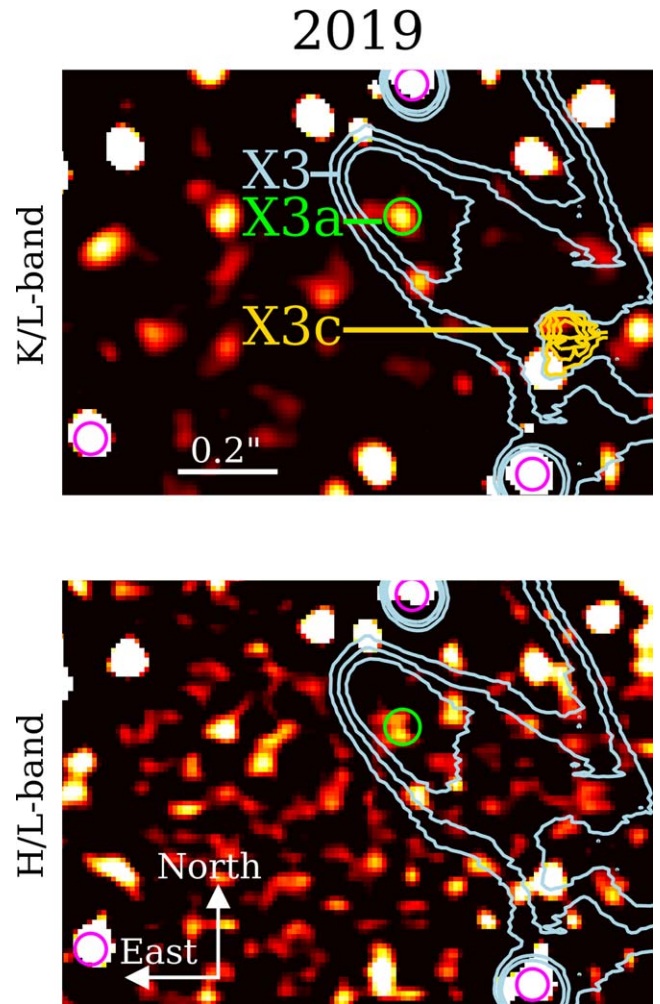


Figure 6. Multiwavelength detection of the X3 system in the *H*, *K*, and *L* bands with NIRC2 (KECK) in 2019. The upper panel shows a combination of the *K* band (background image) and the *L* band (light-blue contours). The lower panel shows the *H*-band emission whereas the light-blue-colored contours are again indicating the *L*-band emission of the bow shock X3. The green circle is placed at the identical position showing the *H*- and *K*-band emission X3a. The blob X3c is hinted by the golden contours above S3-374, which together with S3-373 and S3-375 is indicated by a magenta-colored circle (see Figure 1). No emission of X3b above the noise level is detected at the expected position. We refer the interested reader to the evolution of X3a and X3b shown in Figure 20, Appendix B. Please also consider the setup of the X3 system in 2002 as observed with NACO (Figure 2).

the VISIR data is lower ($\sim 0''.1$) compared to the NACO data ($\sim 0''.027$), the elongation of the bow shock X3 should be detectable. We measure a rough size of about $0''.8$ in the *M* band for the dusty emission associated with X3 (see Figure 10) whereas the SIVr2 line exhibits an FWHM of $0''.3$. Hence, we expect an emission almost three times larger for the lines observed with VISIR if the MIR dust emission matches the distribution of the SIVr2 line. In contrast, the observations show that the MIR emission lines arise from a very dense and compact region that does not exhibit any elongation (please see also Appendix B, Figure 22).

To cover longer-wavelength regimes compared to the IR observations, we display the results of some of the ALMA observation campaigns targeting the vicinity of Sgr A*. The presented radio data are also analyzed in Tsuboi et al. (2017, 2019, 2020a, 2020b) where the authors investigate, among other things, the IRS 13 cluster in detail. In Figure 11,

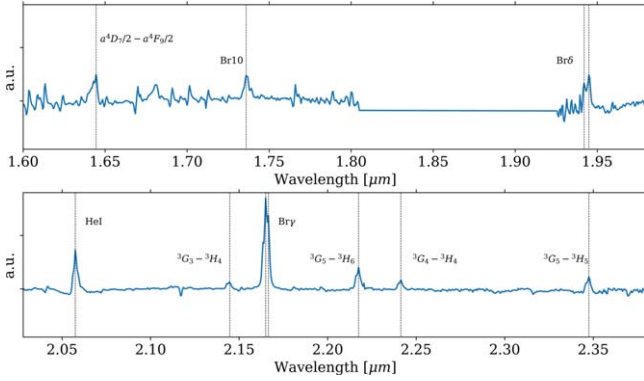


Figure 7. Spectrum ($H+K$ band) of the X3 system extracted from the SINFONI data observed in 2014. Because of different line strengths, we subdivide the spectrum into two subplots (top and bottom). The emission shows tracers such as a double-peaked $\text{Br}\gamma$ line around $2.1661 \mu\text{m}$ and a P Cygni profile close to the blueshifted He I line at $2.0575 \mu\text{m}$. We find no significant NIR CO tracers, which exclude an evolved late-type nature of X3a. We will discuss the missing CO absorption lines in detail in Section 4.

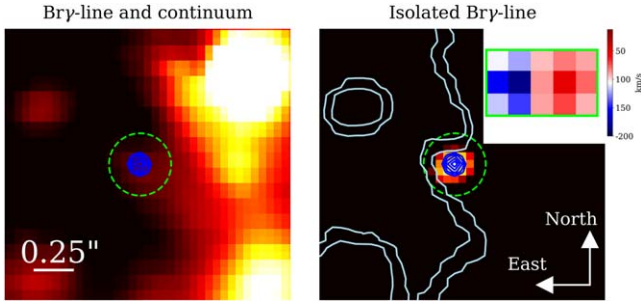


Figure 8. Combined continuum and $\text{Br}\gamma$ line emission observed with SINFONI. The left plot shows the $\text{Br}\gamma$ emission in combination with the continuum (indicated by the surrounding gas and stellar emission). The right image shows a 3 pixel smoothed isolated $\text{Br}\gamma$ line where we subtracted the continuum. For the isolated $\text{Br}\gamma$ line on the right, we integrate over the full width of the double-peaked emission shown in Figure 7. For the blue contour lines, we adapt the normalized emission of the shown isolated $\text{Br}\gamma$ -line corresponding to 50%, 60%, 70%, 80%, and 90% of the peak intensity. In the upper right, we show a position–position–velocity diagram at the position of the double-peak $\text{Br}\gamma$ line. The velocity range is about $\Delta v \simeq 200 \text{ km s}^{-1}$. Additional material shows the velocity gradient and the related offset of the blue- and redshifted $\text{Br}\gamma$ line. A short animation showing the double-peak $\text{Br}\gamma$ line is available. The animation repeats the sequence but with a green circle to highlight the $\text{Br}\gamma$ line. The real-time duration of the animation is 4 s.

(An animation of this figure is available.)

we display the radio/submillimeter emission at the position of X3a. In the same figure, we incorporate the contour lines of the stellar emission X3a (lime colored) and the dust envelope (light-blue colored). The CO emission originates at the stellar position, whereas the $\text{H}30\alpha$ line is distributed around X3a in a ring-like structure as it has been recently observed for the isolated massive YSO G28.20–0.05 by Law et al. (2022). Compared to the downstream bow-shock section, the $\text{H}30\alpha$ emission at the tip of the bow shock is enhanced by $\sim 20\%$. This increased flux density at the position of the bow-shock front implies heating caused by the interaction of X3 with the ambient medium. Taking into account the ALMA observations presented in Figure 11 and considering the SINFONI/VISIR line observations, it is evident that the ionized gas species seem to originate at different components inside the X3 system.

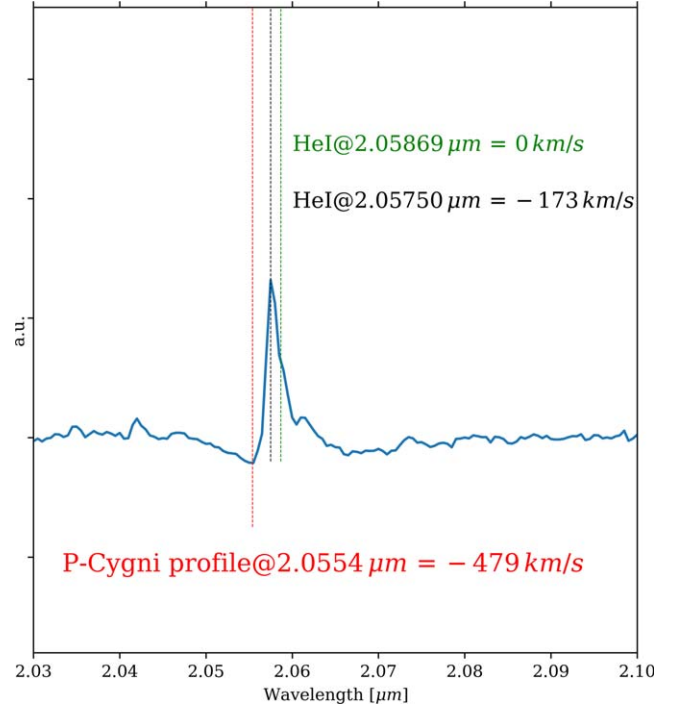


Figure 9. P Cygni profile of X3a observed with SINFONI. The infrared He I (transition $2p^1P^0-2s^1S$) line with a rest wavelength of $2.0586 \mu\text{m}$ is marked with a green dashed line. The spectrum of X3a exhibits a blueshifted He I line with a related line-of-sight velocity of -173 km s^{-1} . Furthermore, a P Cygni profile at $2.0554 \mu\text{m}$ with -479 km s^{-1} is clearly traceable.

3.3. Photometric Analysis

In this subsection, we present the results of the photometric analysis. Since Gautam et al. (2019) find that more than 50% of their star sample (about 570) located in the NSC are variable, we are limited in our selection of a proper reference star that is used to estimate the magnitudes and flux densities of the X3 system. Hence, variability but also fluctuating extinction values (Peißker et al. 2020c) confront the analysis with uncertainties that need to be targeted. Because the bright and close-by members E1, E2, and E3 of the IRS 13 cluster show varying extinction in all investigated bands (see Figure 1 and Mužić et al. 2008; Fritz et al. 2011), we will address these fluctuations using an asymmetric uncertainty range for the estimated magnitude and flux densities (Table 5). Furthermore, we used the most observed object in the NSC, the S-cluster star S2 as a calibration source for the K band whenever possible. Including the H band, we note that the flux analysis of S2 in the literature shows inconsistencies. Therefore, we fit a blackbody SED to the emission of S2 with known individual numerical results (Table 4) for the K (Sabha et al. 2012), L , and M bands (both values are taken from Viehmann et al. 2006). For the SED model presented in Figure 28 (Appendix F), we implement common B2V stellar-type parameters of $R = 8.5 R_{\odot}$ and $T_{\text{eff}} = 22,500 \text{ K}$ (see also Hanson et al. 1996). From the fit, we derive a flux density of $32.0 \pm 0.2 \text{ mJy}$ with the related magnitude of 16.0 mag (Schödel et al. 2010; Peißker et al. 2020b) for the S-cluster star S2 in the H band. For MIR analysis, we include the PAH1 and NeII emission of the close-by reference source IRS 2L (Bhat et al. 2022) and the relation

$$\text{mag}_{\lambda} = -2.5 \times \log(f_{\lambda}/f_0), \quad (2)$$

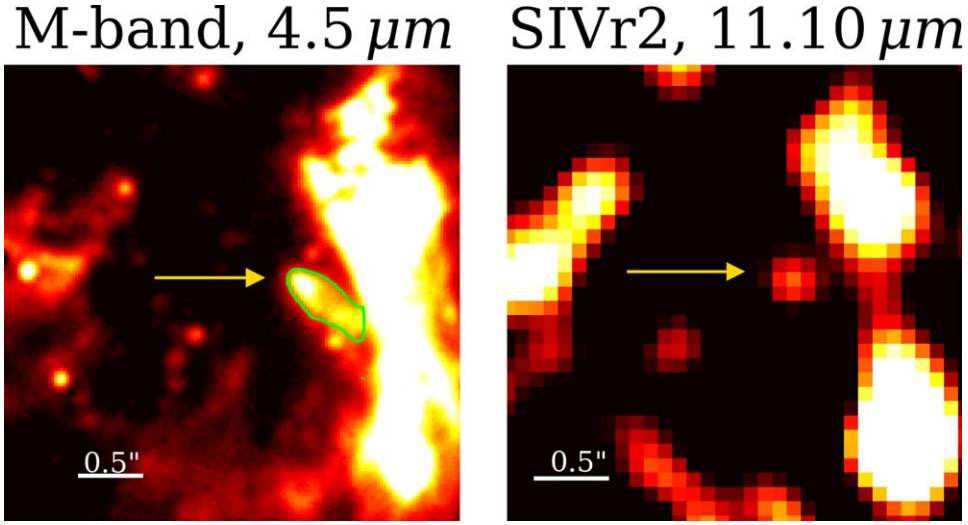


Figure 10. Comparison of the *M*-band continuum with the SIVr2 line emission of X3. The left image was observed with NACO in 2012, and the right image shows observations carried out with VISIR in 2004. The golden colored arrow indicates the position of X3, the *M*-band observations exhibit lime-colored contour lines of the bow-shock source at 35% of the peak emission (see Table 5). The length of the bow shock observed at $4.5 \mu\text{m}$ is about $0''.8$ measured from tip to tail, and the FWHM of the SIVr2 line emission is about $0''.3$. Here, north is up, east is to the left.

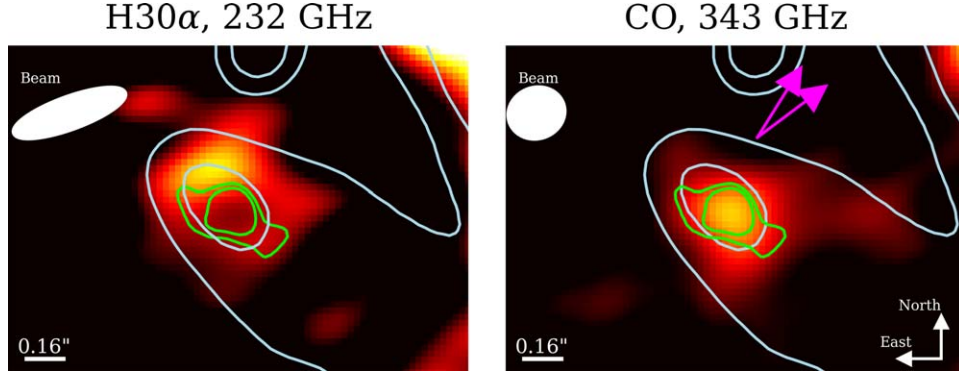


Figure 11. Gas emission observed with ALMA overlaid with *K*- and *L*-band contour lines of X3a and X3. With lime-colored contours, we indicate the *K*-band peak emission of 2.8 mJy at 20% and 40% for X3a as observed in 2015 (see Table 5). With light-blue contours, the *L*-band dust emission of X3 of the same epoch is shown. The background image was observed with ALMA and shows $\text{H}30\alpha$ and CO radio/submillimeter continuum emission at the position of X3a. While the $\text{H}30\alpha$ line seems to be arranged in a ring-like structure around X3a following the morphology of the recently observed massive protostar G28.20–0.05, the CO line exhibits a compact density distribution. Please note that the *K*-band contours do not imply the true size of the stellar source X3a. In the right figure, we show the proper-motion vector with a velocity of about $244 \pm 27 \text{ km s}^{-1}$ (magenta colored, Figure 4).

Table 3
Emission Lines Extracted from the SINFONI (NIR) Data Cube of 2014

Spectral Line (@Rest Wavelength (μm))	Transition	Central Wavelength (μm)	Velocity (km s^{-1})
[Fe II]@1.6440 μm	$a^4D_{7/2} - a^4F_{9/2}$	1.6445 ± 0.0002	91
Br10 @1.7366 μm	$n = 10-4$	1.7360 ± 0.0002	-104
Br δ @1.9450 μm	$n = 8-4$	1.9419 ± 0.0002	-478
He I @2.0586 μm	$2p^1P^0 - 2s^1S$	2.0554 ± 0.0002	-479
He I @2.0586 μm	$2p^1P^0 - 2s^1S$	2.0575 ± 0.0002	-173
H_2 @2.1218 μm	$v = 1-0 \text{ S}(1)$	2.1232 ± 0.001	198
Br γ @2.1661 μm	$n = 7-4$	2.1650 ± 0.0002	-152
Br γ @2.1661 μm	$n = 7-4$	2.1665 ± 0.0002	55
[Fe III]@2.1451 μm	$^3G_3 - ^3H_4$	2.1447 ± 0.0002	-56
[Fe III]@2.2178 μm	$^3G_5 - ^3H_6$	2.2175 ± 0.0002	-41
[Fe III]@2.2420 μm	$^3G_4 - ^3H_4$	2.2414 ± 0.0002	-80
[Fe III]@2.3479 μm	$^3G_5 - ^3H_5$	2.3475 ± 0.0002	-51

Note. We list the rest wavelength of the related emission line. Furthermore, we indicate the transition of the investigated species. The uncertainty of the derived Doppler-shifted velocity is about $\pm 25 \text{ km s}^{-1}$.

Table 4
Derredened Reference Values for S2 and IRS 2L Used in This Work

Band	Magnitude (mag)	Flux _λ (Jy)	References
<i>H</i>	16.0	0.032	S2, see text
<i>K</i>	14.1	0.0147	S2, Sabha et al. (2012)
<i>L</i>	6.4	2.98	IRS 2L, Viehmann et al. (2006)
<i>M</i>	5.5	3.98	IRS 2L, Viehmann et al. (2006)
PAH1	0.9	21.4	IRS 2L, Bhat et al. (2022)
Ne II	0.4	18.9	IRS 2L, Bhat et al. (2022)

Note. The related references are listed (see also Viehmann 2007). For PAH1 and Ne II, we use a zero flux of 50 Jy and 28.6 Jy, respectively (Tokunaga & Vacca 2007).

where mag_λ is the magnitude of the related band and f_0 is the zero flux adapted from Tokunaga & Vacca (2007).¹⁶ With the magnitude and flux information, we photometrically analyze almost 20 yr of observations of the GC using

$$F_\lambda = F_0 \times 10^{(-0.4(\text{mag}_2 - \text{mag}_1))}, \quad (3)$$

where mag_2 refers to the investigated object and mag_1 to the reference source. The resulting magnitudes and fluxes are listed in Table 5. The *H*-, *K*-, *L*-, and *M*-band data are observed with NACO, the narrow filter PAH1, and Ne II with VISIR. We adapt the listed averaged *L*-band magnitude of 9.0 mag from Table 5 to estimate the *L*-band magnitude of X3c. With Equation (2), we calculate an averaged *L*-band magnitude of 10.6 ± 0.6 for X3c. The uncertainties are adapted from the averaged *L*-band magnitude of X3 and represent the standard deviation of the individual measurements per epoch.

3.4. Spectral Energy Distribution

Due to the robust *H*- and *K*-band detection of X3a between 1995 and 2020 (see Figures 2, 20, and 23), the rich line emission in various bands, and the strong outflow that might emerge from the star or a protoplanetary disk (Figure 9), the question about the stellar nature of the object arises. At this point, we can exclude a late-type stellar nature due to the missing infrared CO band heads at 2.29, 2.32, 2.35, and 2.38 μm . The absence of these absorption features clearly separates X3a from late-type stars (Buchholz et al. 2009). We address the question about the nature of X3a with the support of the 3D Markov Chain Monte Carlo radiative transfer code HYPERION to model the composite SED of the X3 system (Robitaille 2011); see also Zajaček et al. (2017) for a similar set-up. For HYPERION, we assume that X3a is a YSO motivated by the above arguments. The 3D dust continuum radiative transfer code calculates individual spectra and allows for a variety of input parameters. From the observed magnitudes and flux densities of X3a, we arrange the input spectrum for HYPERION as the flux density (in Jansky) as a function of wavelength (in microns). See Table 5 for the numerical values of the related input spectrum. This spectrum is then combined with the input values of the model listed in Table 6. We choose 10^6 photons and 10^4 ray-tracing sources, resulting in an average computation time of 12–24 hr per simulation run. In total, we used more than 100 different setups

to derive suitable best-fit parameters for the emission of the X3 system. For example, we checked different stellar-mass assumptions between 0.5 and $25 M_\odot$ in steps of $1 M_\odot$. The results of the model are shown in Figure 12. Among the best-fit parameters are a stellar mass of $15 M_\odot$ with a related effective temperature of 24×10^3 K for X3a. Considering the values listed in Table 5, we transfer the uncertainties of the estimated magnitudes and flux densities of X3 to the comparison plot. Due to the logarithmic scaling of Figure 12, these uncertainties are about the size of the symbols used. Since the uncertainties do not entirely reflect the data distribution, we constrain the mass of X3a to $15_{-5}^{+10} M_\odot$. Consistent with the previous study by Mužić et al. (2010), we independently constrain an inclination angle between $77^\circ.5$ and $87^\circ.5$ for the X3 system. When comparing the mass and luminosity of the X3 system with the GAIA YSO survey, a source with comparable characteristics is identified as MWC 297 (Wichittanakom et al. 2020). We note that the YSO MWC 297 is classified as a Herbig Ae/Be star, which will be adapted for the X3 system. Using the derived mass and the effective temperature of the star, we use the PARSEC code output files (Bressan et al. 2012) to elaborate on the Hertzsprung–Russell diagram (Figure 13). Taking into account evolutionary paths of pre-main-sequence stars of different masses, we can estimate the age of X3 to be ~ 0.04 Myr. The projected stagnation radius of $R_{\text{BS}} \sim 0''.4 \sim 3300$ au, which is close to the deprojected value due to the high inclination, allows us to estimate the mass-loss rate of X3. For this, we use the ram-pressure equilibrium relation (e.g., Wilkin 1996)

$$R_{\text{BS}} = (\dot{m}_w v_w / [4\pi \mu m_{\text{H}} n_a v_{\text{rel}}^2])^{1/2}, \quad (4)$$

where the ambient number density $n_a \sim 26 \text{ cm}^{-3}$ is close to the Bondi radius (Baganoff et al. 2003). The terminal stellar-wind velocity $v_w \sim 400 \text{ km s}^{-1}$ is adapted from the He I P Cygni profile (Figure 9), and the relative velocity with respect to the ambient medium can be approximated by $v_{\text{rel}} \gg v_* \gtrsim 1000 \text{ km s}^{-1}$ due to the nearly perpendicular orientation of the bow shock with respect to the proper-motion vector (Figure 11). From the above numerical approach, we obtain $\dot{m}_w \sim 2.65 \times 10^{-6} - 1.06 \times 10^{-5} M_\odot \text{ yr}^{-1}$. This result is at the higher end of typical mass-loss rates for Herbig Ae/Be stars (Nisini et al. 1995) and is comparable to the input accretion rate for the HYPERION SED calculation. We note that the estimate is strongly dependent on the exact value of the relative velocity value and on the bow-shock stagnation radius.

Furthermore, the stellar orbital velocity of X3a can be estimated simply as $v_* \simeq (v_{\text{LOS}}^2 + v_{\text{PROP}}^2)^{1/2}$, where v_{LOS} defines the LOS velocity and v_{PROP} is the velocity related to the proper motion. With $v_{\text{PROP}} = 244 \pm 27 \text{ km s}^{-1}$ from the fit shown in Figure 4 and the Br γ -based line center LOS velocity of $v_{\text{LOS}} \sim (v_{\text{blue}} + v_{\text{red}})/2 \sim -48.5 \text{ km s}^{-1}$, we obtain the estimate of the stellar orbital velocity of X3a, $v_* = 249 \text{ km s}^{-1}$. The mean orbital distance then is $d_{\text{X3}} \simeq GM_{\text{SgrA*}}/v_*^2 \simeq 0.28 \text{ pc}$, which is slightly larger than the projected distance of $\sim 0.1 \text{ pc}$ of the X3 system from Sgr A*. This is expected due to the inclined stellar orbit with a non-zero LOS velocity traced in the emission lines.

For the modeled SED, we assumed the presence of a massive protoplanetary disk with a related radius of $\lesssim 700$ au around the star. If the double-peak Br γ line originates in the inner disk, which gets spatially extended by outflows, the characteristic Keplerian velocity is estimated to be $v_{\text{Br}\gamma, \text{K}} \gtrsim 103.5 \text{ km s}^{-1}$, which serves as a lower limit for the Keplerian velocity in the

¹⁶ Tokunaga & Vacca (2007) use Vega as a zero-magnitude star.

Table 5
Results of the Photometric Multiwavelength Analysis of X3

Year (YYYY)	<i>H</i> Band		<i>K</i> Band		<i>L</i> Band		<i>M</i> Band		PAH1		Ne II	
	(mag)	(mJy)	(mag)	(mJy)	(mag)	(Jy)	(mag)	(Jy)	(mag)	(Jy)	(mag)	(Jy)
2002	19.6 ^{+0.7} _{-0.3}	1.1 ^{+0.4} _{-0.5}	16.3 ^{+0.7} _{-0.3}	1.9 ^{+0.6} _{-0.9}	9.8 ^{+0.8} _{-0.3}	0.13 ^{+0.03} _{-0.07}
2003	15.8 ^{+0.7} _{-0.3}	3.0 ^{+1.0} _{-1.4}	9.9 ^{+0.8} _{-0.3}	0.11 ^{+0.04} _{-0.06}
2004	19.2 ^{+0.7} _{-0.3}	1.6 ^{+0.6} _{-0.7}	15.8 ^{+0.7} _{-0.3}	3.0 ^{+1.0} _{-1.4}	9.9 ^{+0.8} _{-0.3}	0.11 ^{+0.04} _{-0.06}	3.0 ^{+0.3} _{-0.3}	3.1 ^{+0.9} _{-0.7}	1.4 ^{+0.3} _{-0.3}	7.5 ^{+2.4} _{-1.8}
2005	15.5 ^{+0.7} _{-0.3}	3.0 ^{+1.3} _{-0.9}	9.7 ^{+0.8} _{-0.3}	0.14 ^{+0.04} _{-0.07}
2006	9.6 ^{+0.8} _{-0.3}	0.15 ^{+0.05} _{-0.08}
2007	15.9 ^{+0.7} _{-0.3}	2.8 ^{+0.9} _{-1.4}	9.5 ^{+0.8} _{-0.3}	0.17 ^{+0.05} _{-0.09}
2008	16.0 ^{+0.7} _{-0.3}	2.5 ^{+0.8} _{-1.2}	9.4 ^{+0.8} _{-0.3}	0.18 ^{+0.06} _{-0.09}
2009	15.9 ^{+0.7} _{-0.3}	2.8 ^{+0.9} _{-1.4}	9.3 ^{+0.8} _{-0.3}	0.20 ^{+0.07} _{-0.10}
2010	15.7 ^{+0.7} _{-0.3}	3.3 ^{+1.1} _{-1.5}	8.9 ^{+0.8} _{-0.3}	0.29 ^{+0.10} _{-0.15}	2.4 ^{+0.3} _{-0.3}	5.3 ^{+1.7} _{-1.3}	1.5 ^{+0.3} _{-0.3}	6.8 ^{+2.2} _{-1.6}
2011	15.8 ^{+0.7} _{-0.3}	3.0 ^{+1.0} _{-1.4}	8.4 ^{+0.8} _{-0.3}	0.47 ^{+0.15} _{-0.25}
2012	19.2 ^{+0.7} _{-0.3}	1.6 ^{+0.6} _{-0.7}	15.8 ^{+0.7} _{-0.3}	3.0 ^{+1.0} _{-1.4}	8.4 ^{+0.8} _{-0.3}	0.47 ^{+0.15} _{-0.25}	7.9 ^{+0.7} _{-0.3}	0.43 ^{+0.14} _{-0.24}
2013	8.7 ^{+0.8} _{-0.3}	0.35 ^{+0.12} _{-0.18}
2014
2015	15.9 ^{+0.7} _{-0.3}	2.8 ^{+0.9} _{-1.4}	8.5 ^{+0.8} _{-0.3}	0.43 ^{+0.13} _{-0.23}
2016	8.4 ^{+0.8} _{-0.3}	0.47 ^{+0.15} _{-0.25}	2.0 ^{+0.3} _{-0.3}	7.7 ^{+2.3} _{-1.8}	1.3 ^{+0.3} _{-0.3}	8.2 ^{+1.8} _{-2.0}
2017	8.4 ^{+0.8} _{-0.3}	0.47 ^{+0.15} _{-0.25}
2018	15.9 ^{+0.7} _{-0.3}	2.8 ^{+0.9} _{-1.4}	8.2 ^{+0.8} _{-0.3}	0.56 ^{+0.18} _{-0.29}	2.0 ^{+0.3} _{-0.3}	7.7 ^{+2.3} _{-1.8}	1.3 ^{+0.3} _{-0.3}	8.2 ^{+1.8} _{-2.0}
2019	19.6 ^{+0.7} _{-0.3}	1.1 ^{+0.4} _{-0.5}	16.1 ^{+0.7} _{-0.3}	2.3 ^{+0.7} _{-1.0}
2020	16.0 ^{+0.7} _{-0.3}	2.5 ^{+0.8} _{-1.2}
Averaged	19.4 ± 0.2	1.4 ± 0.3	15.9 ± 0.2	2.8 ± 0.4	9.0 ± 0.6	0.29 ± 0.15	7.9 ± 0.5	0.43 ± 0.1	2.3 ± 0.4	5.9 ± 1.9	1.3 ± 0.1	7.7 ± 0.6

Note. Please note that all flux densities are given in Jansky except for the *H* and *K* bands. Lower magnitude values are brighter while higher flux densities are associated with stronger source emission.

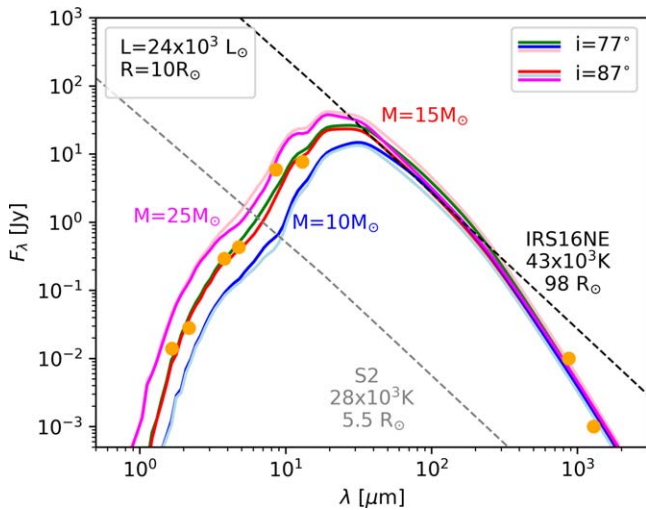


Figure 12. Spectral energy distribution of the X3 system in comparison with early-type stars. We show the flux density in Jansky as a function of wavelength in microns with a logarithmic axis scaling. The inclination angles of 77° and 87° with a related stellar mass of $15M_\odot$ are marked with green and red, respectively. The (light) blue lines indicate the lower stellar-mass limit of $10M_\odot$. In contrast, magenta/pink shows the upper mass limit of $25M_\odot$, resulting in a final stellar-mass estimate of $15^{+5}_{-10}M_\odot$. The estimated flux densities are represented by orange dots whereas the size correlates with the uncertainties. The gray and black dashed lines represent the blackbody SED fits of S2 and IRS 16NE, respectively (Krabbe et al. 1995; Habibi et al. 2017).

Table 6
Final Input Parameters for HYPERION

Properties	Setting
Radius [R_\odot]	10
Luminosity [L_\odot]	24×10^3
Mass [M_\odot]	15
Disk mass [M_\odot]	0.01
Disk radius (min) [R_\odot]	50
Disk radius (max) [au]	700
Disk radius height [R_\odot]	0.01
Accretion [$M_\odot \text{ yr}^{-1}$]	10^{-6}
Ulrich env. (min) [R_\odot]	50
Ulrich env. (max) [au]	1000
Number of Photons	10^6
Ray-tracing sources	10^4
Number of Iterations	10

Note. In addition to these settings, we define an input spectrum related to the derived fluxes listed in Table 5.

disk due to an uncertain inclination (Kraus et al. 2012). The mean radius for the origin of the $\text{Br}\gamma$ -emitting material is $r_{\text{disk,Br}\gamma} \lesssim Gm_{\text{X3a}}/v_{\text{Br}\gamma,\text{K}}^2 \sim 1.2 \text{ au}$. This is in agreement with the orbiting bound ionized material around a YSO that could be either inflowing or outflowing, that is, an accretion or a decretion disk (Alcalá et al. 2014). This provides a consistency test of the overall kinematics of the system (stellar orbital motion around Sgr A* as well as the bound gas motion around the X3a star), which is in agreement with the proposed computational model (Figure 12). We note that the observed $\text{Br}\gamma$ line is spatially extended as is expected for Herbig Ae/Be stars (Tatulli et al. 2007; Davis et al. 2011). We will elaborate on this relation in the following section.

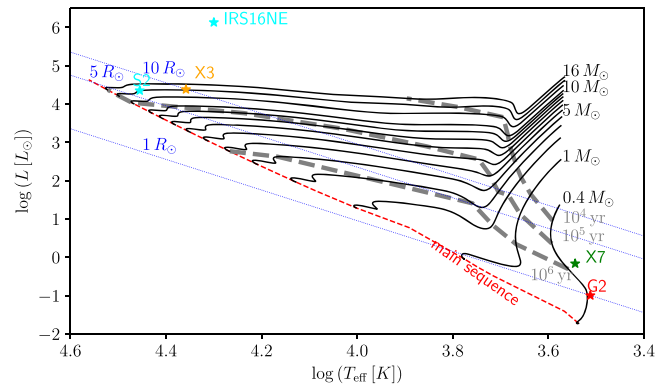


Figure 13. Position of the X3 in the Hertzsprung–Russell diagram. The X3 position (orange asterisk) in the Hertzsprung–Russell diagram is compared with the pre-main-sequence star evolutionary tracks according to the PARSEC code (Bressan et al. 2012), calculated for the near-solar metallicity of $Z = 0.01$. Evolutionary paths of stars in the mass range $1\text{--}10M_\odot$ are shown (with $1M_\odot$ increments) as well as 0.4 , 12 , 14 , and $16M_\odot$ stars are depicted. In addition, we plot 10^4 , 10^5 , 10^6 yr isochrones, the zero-age main sequence, and the lines standing for $1R_\odot$, $5R_\odot$, and $10R_\odot$ (blue dotted lines). The inferred temperature and the luminosity of X3 are consistent with being a pre-main-sequence massive star ($\sim 14\text{--}15M_\odot$ having an age of $\sim 40,000$ yr). For comparison, we also plot the positions of X7 and G2 objects according to the broadband SED fits of Peißker et al. (2021a) and Peißker et al. (2021c), respectively. In contrast to X3, they follow the evolutionary track of a low-mass star of $\sim 0.4M_\odot$ with the age of $\gtrsim 10^6$ yr. The denoted OB stars S2 and IRS 16NE are also clearly offset from the X3 star.

4. Discussion

In the following, we will discuss the various findings of the presented analysis. First, we will summarize the different components related to the X3 system. Second, we will motivate the stellar nature of the bow-shock source. Third, we will propose a speculative scenario to explain the formation process of the young star.

4.1. The X3 System

Analyzing NIR data observed with the VLT and KECK, we trace X3a along with X3 between 2002 and 2020, which is reflected by a matching proper motion of $244 \pm 27 \text{ km s}^{-1}$. In the case of two nonrelated sources, we would expect a significant difference in not only the proper motion but also the trajectory. Considering the statistical analysis of Sabha et al. (2012) for a random flyby event, the 3D motion of X3 and X3a is a six-parameter problem (x , y , v_{pm_x} , v_{pm_y} , v_{los_x} , v_{los_y}) where it is unlikely that at least four parameters are arranged in a way that $x_{\text{X3}} = x_{\text{X3a}}$ and $y_{\text{X3}} = y_{\text{X3a}}$. However, several studies (see, for example, Gallego-Cano et al. 2018) investigate the stellar density as a function of distance from Sgr A*. Hence, we expect by definition that at larger distances, the chance for a random encounter is significantly decreased. Considering the KLF for IRS 13E taken from Paumard et al. (2006), we find for the position of the X3 system in total ~ 8 sources/ $(1'')^2$. Taking into account the spatial pixel scale of NACO, we obtain the mean value of 0.14 sources per resolution element (i.e., pixel). For the almost-consecutive NACO observations between 2002 and 2018, we find a random source at a random position of about 2%. Sabha et al. (2012) and Eckart et al. (2013) estimate a similar value for the higher crowded S-cluster. Considering that a random flyby encounter of two stars dissolves after three years, it becomes negligible that such an event can explain the

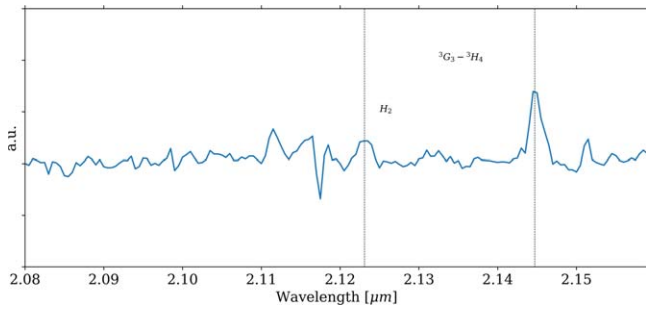


Figure 14. Zoomed-in view of the SINFONI extracted spectrum in the spectral region between 2.08 and 2.155 μm to show the Doppler-shifted H_2 line. Besides the H_2 line at 2.1232 μm (rest wavelength at 2.1218 μm), one forbidden iron transition at 2.1447 μm is indicated. The presence of the Doppler-shifted emission line H_2 with $v_{\text{H}_2} = 198 \text{ km s}^{-1}$ observed with SINFONI is an indicator of the presence of a protoplanetary disk (Glassgold et al. 2004). For the related line map of the H_2 detection, please consult Figure 27, Appendix E.

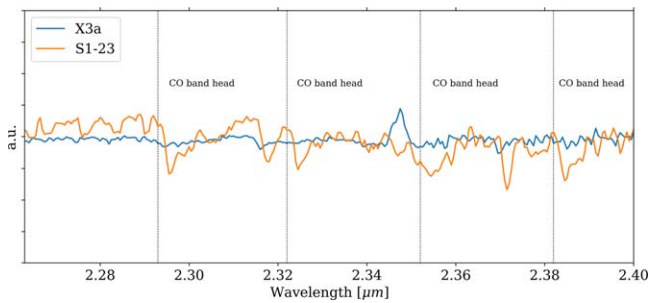


Figure 15. Search for IR CO band heads for X3a and comparison with the late-type analog S1-23. For the identification of the late-type star S1-23, we use the spectral analysis of Gautam et al. (2019).

comovement of the H -, K -, and L -band detection of X3 and X3a.

Regarding X3b, it is reasonable to assume that the thermal blob was created (or confused) between 1995 and 2002 and disappeared around 2012. While the ejection of a blob from the central stellar source X3a is rather speculative, the formation of dense material within the bow shock due to instabilities is supported by simulations of bubbles around the bow-shock tip (Gardner et al. 2016) and observations (Maureira et al. 2022). We can assume that unstable bubbles suffer from magnitude and flux variations because of their nature. Investigating the K -band magnitude of X3b in 2002 revealed a magnitude of about 16 mag, which was higher compared to X3a (see Table 5). Since no emission above the noise of X3b is detected in 2012, we compare this magnitude to the NACO detection limit of 18.5 mag and find therefore a decrease of $\Delta_{\text{mag}} = 18.5 - 16.0 = 2.5$. Therefore, the analysis implies that X3b suffered a decrease in thermal energy between 2002 and 2012 due to radiative or adiabatic cooling, which justifies the classification as a thermal blob. Furthermore, the proper motion of X3a observed in the H and K band is in reasonable agreement with X3, which suggests that both sources belong to the same system. This argumentation is also valid for X3c although the nature of the compact blob is challenging to uncover. The X3c component could be related to the collimated bow-shock downstream flow, such as within the Bondi–Hoyle–Lyttleton (BHL) accretion flow model (Matsuda et al. 2015). This mechanism describes the shock-formation downstream at a specific stagnation point. Taking into account the thermal

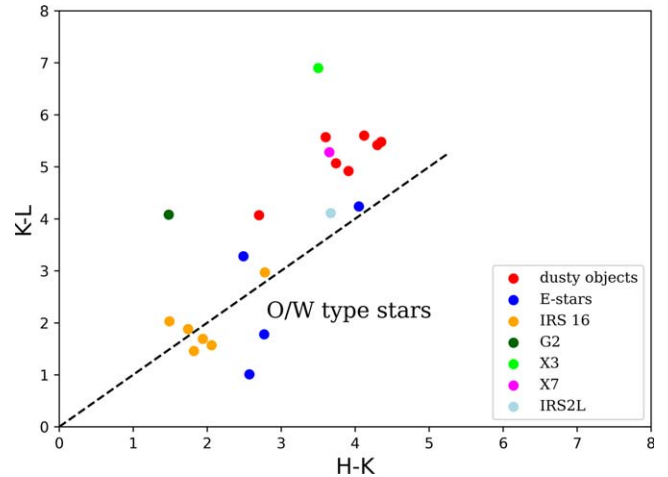


Figure 16. Color-color diagram of close-by sources. We use published $H - K$ and $K - L$ colors of close-by sources (Eckart et al. 2004; Viehmann et al. 2006) and incorporate the estimated magnitudes for X3 (Table 5), X7 (Peißker et al. 2021a), and G2 (Peißker et al. 2021c). The dashed line represents an emitting blackbody at different temperatures. The presumed YSOs exhibit a higher $K - L$ color compared to the O/W-type stars in our sample.

pressure of the ambient hot plasma as discussed in Christie et al. (2016), it is also plausible that the surrounding medium could create enough pressure to make the bow-shock shell closed and X3c would be the shock formed where the streams meet. As a consequence, the blob is expected to be variable and the material could be accreted over time. Although we did not find indications of an accretion process between 2002 and 2018 (see Figure 5), it could be subject to future observations. However, the idea of high thermal pressure to explain the nature of X3c seems appealing since the cigar shape of X7 (Peißker et al. 2021a) could also be created by a dominant thermal pressure of the ambient medium.

4.2. The Nature of X3a

Examining the different Doppler-shifted velocities for X3 as observed with SINFONI, it is implied that various components of the system are responsible for the emission. For example, the observed $\text{Br}\gamma$ emission (Figure 8) exhibits a double-peak line that shows a velocity gradient along the source, implying the presence of a disk or strong outflows (Davis et al. 2011). We will discuss this particular feature in Section 4.3. Furthermore, the He I line might be connected to outflows from a possible jet or strong stellar winds (see the P Cygni profile shown in Figure 9). Helium pumping can be considered to be the responsible mechanism for the forbidden iron multiplet (Peißker et al. 2021a). We note the detection of a Doppler-shifted H_2 line (Figure 14), which might serve as an additional tracer for photoionized outflows originating close to the massive protostar X3a (Kumar et al. 2002; Tanaka et al. 2016). The detection of the NIR H_2 line is accompanied by the radio/submillimeter CO emission presented in Figure 11. Both lines are common indicators for the presence of a protoplanetary disk and outflows of Herbig Ae/Be stars (Thi et al. 2001; Davis et al. 2011). Although the spatial resolution of SINFONI forbids a detailed determination of the exact origin of the H_2 emission line, the arrangement of the ionized CO and $\text{H}30\alpha$ line observed with ALMA and displayed in Figure 11 suggests different origins of the detected gas species related to the X3 system. To exclude the possibility of a stellar

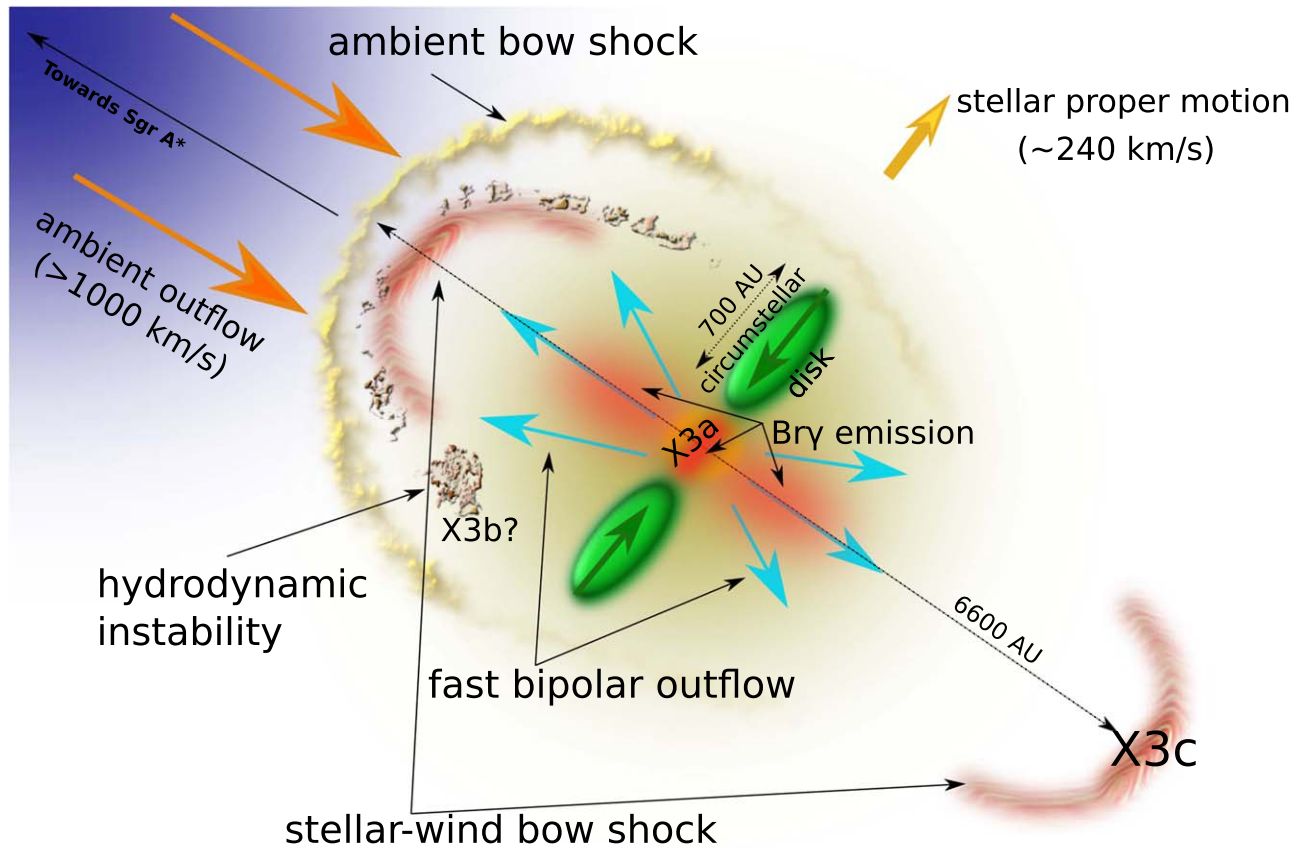


Figure 17. Sketch of the X3 system. The figure depicts the central massive star X3a that is surrounded by the circumstellar disk (green), whose inner ionized part and the associated disk outflows (blue) emit $\text{Br}\gamma$ emission (reddish regions). The stellar and disk outflows get shocked within the stellar-wind bow shocks. The downstream bow shock may be associated with the stable infrared continuum component X3c. Since the star moves supersonically with respect to the ambient medium, a bow shock forms in the ambient medium as well (yellow). The inner (stellar wind) and outer (ambient medium) bow-shock shells mix together and hydrodynamic instabilities form downstream. The transient infrared component X3b might be associated with a larger instability formed downstream. Yellow and orange arrows indicate the stellar proper motion and the ambient outflow directions, respectively, including their inferred velocities. Not drawn to scale.

classification as late type, we inspect the SINFONI spectrum for CO absorption lines, which are typical for evolved stars. Consequently, young stars do not show extended infrared CO band heads between 2.3 and $2.4 \mu\text{m}$. To visualize the difference of the CO band heads for different stellar ages, we compare the SINFONI spectrum of X3a with the late-type star S1-23, which is located about $2''.36$ east of IRS 13 (Gautam et al. 2019). In Figure 15, the two spectra of both sources are incorporated and the CO band-head locations are marked. Due to the absence of the CO band-head features in the X3a spectra, the stellar temperature must be higher compared to S1-23. From the normalized spectrum presented in Figure 15, we evaluated the depth of the CO band (CBD) using the feature at $2.36 \mu\text{m}$. We follow the analysis of Buchholz et al. (2009) and derive a CBD for X3a of -0.1 , for S1-23 a value of 0.4 . From a critical point of view, the CBD might be biased by telluric correction, background, or noise level. However, the CBD is only considered to provide a rough classification that separates late-type stars from young stellar sources and serves as an independent parameter that underlines our findings for X3a.

This classification is supported by the broadband SED with a prominent NIR and MIR excess, the double-peak profile of the $\text{Br}\gamma$ line with the velocity gradient of $\sim 200 \text{ km s}^{-1}$ indicating a rotating structure or outflows, and the prominent P Cygni profile of the He I emission line. Therefore, we conclude that the X3 system can be described as a YSO with a protoplanetary

disk embedded in a bow-shock dust envelope. With the support of stellar evolutionary tracks shown in Figure 13, we propose that X3a is a young Herbig Ae/Be star with a mass of $15_{-5}^{+10} M_{\odot}$ and an estimated age of a few 10^4 yr. Estimating the $H - K$ and $K - L$ colors from Table 5 and comparing them with the surrounding stars and dusty objects of the nearby cluster IRS 13, we find further support for the pre-main-sequence nature of X3a (see Figure 16). To get a better understanding of the setup of the X3 system, we display a possible arrangement for the different components (protostar, protoplanetary disk, dust envelope, bow shocks) in the sketch shown in Figure 17.

We note that this sketch is not to scale, but it captures the main components and dynamics of the X3 system. In particular, the interaction of the stellar and disk outflows (Figure 9) leads to the formation of two bow shocks, one of which (downstream one) may be associated with the stable infrared continuum component X3c. Furthermore, due to the supersonic motion of X3a with respect to the ambient medium, a bow shock forms in the ambient medium as well and the shocked gaseous-dusty material flows downstream, giving rise to the elongated shape of the X3 system visible in the L band. Due to several molecular and recombination-line tracers, the X3a star is surrounded by a circumstellar disk (~ 700 au) in radius, whose inner part is ionized and is the source of the double-peaked $\text{Br}\gamma$ line. The $\text{Br}\gamma$ emission is further extended above and below the disk plane due to bipolar disk winds. The

whole model may be even more complex, e.g., due to the presence of the so-called transition disk that connects the dust envelope with the accretion disk (Haworth et al. 2016). Such a transition area also increases the size of an accretion disk compared to the sketch shown in Figure 17. Recent observations of (massive) YSOs suggest the existence of this feature which extends possible disk sizes (Frost et al. 2019; GRAVITY Collaboration et al. 2020). While it can be argued that additional background noise may impose uncertainties that increase the confusion in order to estimate the exact disk size (Figure 8), observations of massive YSOs in the Carina Nebula revealed even larger disk dimensions compared to the X3 system (Preibisch et al. 2011). Using the settings for the disk radius of the model from Table 6, we estimate an expected size of almost 100 mas, which is in reasonable agreement with the dimensions displayed in Figure 8. In the next section, we will provide a detailed approach to the composition of the X3 system.

4.3. The Disk Structure of the X3 System

In Figure 8, we show the detection of ionized Doppler-shifted Br γ with an FWHM of about 0''15 (\sim 1200 au), which is about the size of the SINFONI PSF (\sim 0''25) for the corresponding spatial plate scale. The diffraction-limited detection of the integrated Br γ line shown in Figure 8 is confined by the resolution of the telescope and indicates that the ionized hydrogen originates in a smaller area than 0''15. In contrast, the single blue- and redshifted line maps (see the PPV diagram in Figure 8 and the attached movie) exhibit a slightly extended size of about 0''25 (\sim 2000 au) that matches the FWHM of the SINFONI PSF.

Although the Br γ line is often used as a tracer for accretion disks, the quantities of the X3 system exceed typical disk sizes of a few 10 to about 100 au (Beck et al. 2010; Beck & Bary 2019). However, Davis et al. (2011) and Ward et al. (2017) show spatially extended Br γ lines of massive YSOs that exceed dimensions of several hundred up to 1000 au. This apparent inconsistency can be explained by photoionized disk-wind outflows and, more generally, stellar winds that increase the spatial distribution of the Br γ line. For example, Kraus et al. (2012) performed VLTI/AMBER observations of Br γ gas distributions and showed that the Doppler-shifted line exhibits a photocenter offset compared to the central emission. Although Kraus et al. (2012) investigate classical Be stars, Tanaka et al. (2016) simulate density distributions n_{H} of hydrogen around massive protostars. Tanaka et al. (2016) report strongly ionized outflows of high-mass protostars with associated temperatures of about 5000–10,000 K on 100–2000 au scales. Since Br γ can be detected at temperatures around 8000 K (GRAVITY Collaboration et al. 2023), the results of Tanaka et al. (2016) are in agreement with the observations carried out by Davis et al. (2011), Ward et al. (2017), and this work. Due to the high mass of the X3 system (Figure 12), it is expected that ionized stellar winds distribute gas species on scales of several hundred astronomical units (Tanaka et al. 2016). This argument follows the analysis of Davis et al. (2011), who interpret the spatially extended Br γ emission as a tracer for outflows, which was independently shown by VLTI/AMBER observations carried out by Tatulli et al. (2007).

Although we cannot spatially resolve the accretion disk of the X3 system, we can safely assume that we observe a superposition of the warm disk material with strongly ionized

outflows that are traced by the detected P Cygni profile. Another mechanism might impose constraints on the detection of the size of the Br γ emission area. As we show in Figure 11, the H3 α line is arranged in a ring-like structure with an approximate diameter of about 0''25 or 2000 au exhibiting a comparable morphology to the massive protostar G28.200.05 observed by Law et al. (2022). The size of the ionized hydrogen matches the Br γ emission but also the MIR lines detected with VISIR (see Figures 10 and 22, Appendix D) and ISAAC (Figure 24, Appendix D), implying that all detected atomic and molecular species originate in the same region. The enhanced intensity of the H3 α line at the tip of the bow shock of about 20% might be related to the interaction of the ambient medium with the X3 system, which is in agreement with the 3D magnetohydrodynamic models of ζ Ophiuchi carried out by Green et al. (2022). The increased temperature in the bow-shock tip caused by the interaction of the supersonic X3 system with the ambient medium could also be responsible for the increased Br γ emission size. Scoville & Burkert (2013), for example, show a spatially increased Br γ emission created by the interaction of a young T Tauri star with the ambient medium around Sgr A*. This contributes to the high temperature within the disk material in combination with the photoionized disk-wind outflows. Because there might be an interplay between the bow-shock-induced temperatures and strong winds, gas flows through the disk cannot be ruled out. A probe for these gas flows is polycyclic aromatic hydrocarbons (PAHs; see Figure 22). We use the SED representing IRS 3 (Figure 1) derived by Pott et al. (2008) to normalize the PAH1 and PAH2 detection (Figure 22, Appendix B) of the X3 system and infer the intensity ratio $I_{\text{PAH1}}/I_{\text{PAH2}}$ of \sim 6. Following the analysis of Herbig Ae/Be stars shown in Maaskant et al. (2014), we can conclude that the PAH total emission can be distributed in a radius around the protostar between a few astronomical units up to 1000 au. The PAH intensity ratio implies gas flows between optical thick disks located close to and farther away from the protostar.

For the X3 system, we can therefore conclude that the presence of a thick accretion disk and an optically thin region of gas flow (Maaskant et al. 2014) or transition disk (Haworth et al. 2016) embedded in an optically thick dust envelope is the most plausible explanation for the observed lines. Strongly ionized outflows are responsible for the spatially extended Br γ emission. The size of the Br γ -confined area matches all other lines detected in this work, in agreement with the hypothesis of dominant photoionized winds. For a visualization of the different components and interplays, please see the sketch displayed in Figure 17.

4.4. The Gravitational Stable X3 System

Although the gravitational footprint of Sgr A* can be traced at a distance of \sim 0.1 pc, the high stellar mass of X3a effectively shields the inner region of the system on the scale of \sim 100 au. To provide a quantitative estimate of the gravitational imprint of Sgr A* on the X3 system, we estimate the tidal radius with

$$r_{\text{t}} \sim R_{\text{X3}}(2M_{\text{SgrA*}}/m_{\text{X3a}})^{1/3}, \quad (5)$$

where $R_{\text{X3}} \sim 0.005$ pc is the approximate size of the X3 bow shock, $M_{\text{SgrA*}} = 4 \times 10^6 M_{\odot}$ is the mass of Sgr A* (Peißker et al. 2022), and m_{X3a} is the mass of X3a (\sim 15 M_{\odot}). Using the above relation, we estimate the tidal radius of $r_{\text{t}} \sim 0.41$ pc,

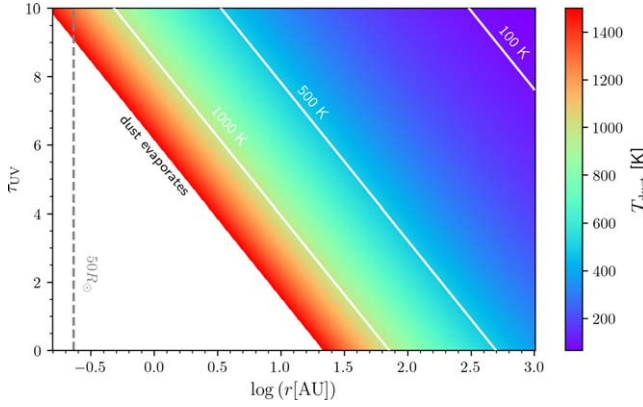


Figure 18. Dependence of the dust temperature T_{dust} on the distance from the X3a star ($\log r$) and the optical depth τ_{UV} of the circumstellar medium at a given distance. The vertical dashed gray line marks the distance of $50R_{\odot}$ for orientation. The contours for 100, 500, and 1000 K are depicted as white solid lines. The white region in the left corner represents the parameter space where $T_{\text{dust}} > 1500$ K.

which is greater than or comparable to the X3 distance from Sgr A*, $d_{\text{X3}} \sim 0.3$ pc (see Section 3.4). Therefore, the outermost bow shock can be affected by the ambient tidal field of Sgr A*. However, the Hill radius of X3a is $r_{\text{Hill}} \sim d_{\text{X3}} [m_{\text{X3a}} / (3M_{\text{SgrA*}})]^{1/3} \sim 700$ au, which implies that the stellar core and the surrounding circumstellar material are bound and not significantly affected by the gravitational field of Sgr A*. The extended sphere of influence of X3a has likely also determined the fate of the thermal warm blob X3b, which disappeared when it reached a comparable distance from X3a. The remnant of X3b will approach the star on the freefall timescale of $t_{\text{ff}} \sim \pi (r_{\text{Hill}}/2)^{3/2} (Gm_{\text{X3a}})^{-1/2} \sim 850$ yr; see also Figure 5. The disappearance of X3b may be related to faster hydrodynamical processes, specifically the interaction with the bound material around the star or the stellar outflow and subsequent shocks.

4.5. Dust Temperature and Sublimation Radius

Given the large bolometric luminosity of the X3a star, $L_{\text{bol}} \simeq 24 \times 10^3 L_{\odot}$, and the stellar radius, $R_{\star} \simeq 10 R_{\odot}$, see Table 6, we obtain the effective temperature of $T_{\star} \simeq 22,700$ K. This implies that the X3a star emits most of its radiation in the UV domain ($\lambda_{\text{max}} \sim 128$ nm) and due to the large luminosity, the circumstellar dust evaporates at the sublimation radius r_{sub} at a certain distance from the star where it reaches the temperature of $T_{\text{sub}} \sim 1500$ K. To estimate r_{sub} , we use the model of Barvainis (1987) for the temperature of the graphite grains at the distance r_{\star} from the star given the UV luminosity L_{UV} of the central source and the optical depth τ_{UV} of the material, in which grains are located. For $L_{\text{UV}} \sim L_{\text{bol}}$, we obtain the dust temperature scaled approximately to the sublimation temperature,

$$T_{\text{dust}} \simeq 1501.3 \left[\left(\frac{L_{\text{UV}}}{24 \times 10^3 L_{\odot}} \right) \left(\frac{r_{\star}}{23 \text{ au}} \right)^{-2} e^{-\tau_{\text{UV}}} \right]^{1/5.6} \text{ K}, \quad (6)$$

hence, if the dust is not shielded, it evaporates at $r_{\text{sub}} \sim 23$ au. At larger distances, colder dust contributes to the mid- and far-infrared thermal emission of the X3 system. The peak in the SED close to $20\text{--}30 \mu\text{m}$, see Figure 12, can be interpreted by

the thermal emission of dust with the temperature of ~ 100 K, which must be shielded from the star by the optically thick circumstellar disk and outflows. If the optical depth reaches values close to $\tau_{\text{UV}} \sim 10$, dust with $T_{\text{dust}} \sim 100$ K is located at $r_{\star} \sim 300$ au according to Equation (6).

A comparable dust sublimation radius is obtained from the numerically determined relation by Whitney et al. (2004),

$$r_{\text{sub2}} = R_{\star} \left(\frac{T_{\text{sub}}}{T_{\star}} \right)^{-2.085}, \quad (7)$$

which gives $r_{\text{sub2}} \sim 289R_{\star} \sim 13.4$ au. Equation (7) takes into account shielding by an optically thick inner disk wall, hence the dust can then exist still closer in comparison with the optically thin limit ($\tau_{\text{UV}} = 0$) evaluated in Equation (6).

In Figure 18, we show the distribution of the dust temperature around the X3a star as a function of the distance from the star (in astronomical units) and the optical depth, using the simplified model of Barvainis (1987) for a single point source with the UV luminosity of $L_{\text{UV}} = 24,000L_{\odot}$. The plot shows a strong dependence of the dust temperature at a given distance on the optical depth, and hence on the shielding by the opaque circumstellar disk and outflows.

4.6. Formation History of X3

As a consequence of this analysis, the presence of a high-mass YSO requires the question of the origin and the formation process of the X3 system to be assessed. We will therefore discuss three different possible scenarios for the formation of the X3 system.

1. For the first scenario, we consider the proposed top-heavy initial mass function for young stars in the GC proposed by Lu et al. (2013). The authors assume a single starburst about 6–7 Myr ago that explains the presence of investigated young stars. Due to the age of the X3 system of ~ 0.04 Myr, this formation scenario can be excluded.
2. The second scenario is proposed by, among others, Jalali et al. (2014). This scenario of inspiraling molecular clouds with masses of about $100 M_{\odot}$ might be appealing since Yusef-Zadeh et al. (2013) already found indications of high-mass-star formation, which was underlined by the observations of Moser et al. (2017) and Hsieh et al. (2021). However, there should be at least some tracers of a recent massive cloud infall, such as elongated gaseous-dust features or trail stars (for further discussion, see also Paumard et al. 2006).
3. The third and the last discussed scenario is a continuous star formation process in the GC. In this scenario, it is believed that ongoing star formation processes take place in the so-called (counter)clockwise disks as proposed by Paumard et al. (2006). Due to high gas and dust temperature (Cotera et al. 1999), the turbulent environment (Genzel et al. 2000), and strong magnetic field, this scenario seems at least questionable. On the other hand, it can explain the variety of stellar members and regions in the inner parsec, such as IRS 13, IRS 16, and early-/late-type stars (Krabbe et al. 1995; Habibi et al. 2017; Gautam et al. 2019). Overdensities in the two disks could have created cluster structures like the mentioned IRS 13 and IRS 16 regions.

We consider a combination of the second and third scenarios as the most plausible explanation for the origin of the X3 system without excluding the starburst scenario as a general concept. Specifically, a cluster of young stars could have started to form outside the inner parsec, e.g., in the region of the current CND, and at the same time, it was migrating toward Sgr A*. Due to cloud–cloud interactions, the initial birthplace of the X3 system could have lost angular momentum. The dynamical instability timescales that are required for the formation of the X3 system are in agreement with Kelvin–Helmholtz timescales as we have shown for a young T Tauri star (Peißker et al. 2021c). As suggested by Maillard et al. (2004), IRS 13 might be an example of an evaporating cluster with ongoing star formation. Maillard et al. (2004) propose that IRS 13 is the remnant core of a massive cluster. As a result, IRS 13 could be the birth site of some of the high-mass stars in the GC as discussed by the authors. Portegies Zwart et al. (2003) favor a similar explanation for the IRS 16 stars as they also propose an inspiral of the cluster caused by dynamical friction.

Taking into account the direction and proper motion of the studied dusty objects of IRS 13 (Eckart et al. 2004), our estimated value of $v_{\text{PROP}} = 244 \pm 27 \text{ km s}^{-1}$ for the X3 system coincides with these presumed YSOs of the cluster (Mužić et al. 2008, 2010). Furthermore, v_{PROP} of X3 matches the proper motion of the evolved WR stars E2 and E4 (Zhu et al. 2020). Therefore, we cannot exclude the possibility that the X3 system might be a cluster member of IRS 13. Considering the young age, X3a must have formed in situ due to the migration timescales (Morris 1993). This implies that IRS 13 could have initially served as the birthplace of the X3 system in agreement with the discussion about the origin of some high-mass stars by Maillard et al. (2004). During the infall of IRS 13, the X3 system might have been separated from the cluster due to tidal disintegration and the initial velocity dispersion of forming stellar cores. This could also explain the spatial offset of about $1''$ between the X3 system and IRS 13. Consequently, the inspiraling and evaporating cluster should have lost more sources similar to X3a (Paumard et al. 2006). Tracers of this event might be the low- and high-mass YSOs observed by Yusef-Zadeh et al. (2013, 2015, 2017) in the inner 2 pc of the GC. If IRS 13 is, however, not classified as a cluster but rather as a fragmented disk structure, the theoretical scenarios proposed by Bonnell & Rice (2008), Hobbs & Nayakshin (2009), and Jalali et al. (2014) that describe the inspiral of massive molecular clouds should be considered to explain the formation of the X3 system. In particular, the simulations by Bonnell & Rice (2008) favor the formation of high-mass stars, which could serve as a plausible explanation for the high-mass YSO described here. While this formation scenario seems appealing, it does not explain the discovery of 11 low-mass bipolar outflow sources by Yusef-Zadeh et al. (2017). These bipolar outflow sources are located in not only the inner parsec, but also the S-cluster as we suggest in Peißker et al. (2019). Recently, Owen & Lin (2023) proposed a new formation path for X8 (Peißker et al. 2019) and similar sources (Ciurlo et al. 2020; Peißker et al. 2020b) that requires the presence of giant planets in the related disk of the young protostar. Although all of the above scenarios aim to explain a specific stellar type or group in the NSC, no approach is able to address the rich presence of various stars of different ages. For example, the young stars in the S-cluster exhibit an age range of $\sim 3\text{--}15$ Myr, clearly inconsistent with the starburst 6 Myr ago (Lu et al. 2013) or an infalling molecular cloud with conjunct star formation processes (Jalali et al. 2014). In the midterm perspective, upcoming GC

observations with the James Webb Space Telescope utilizing MIRI IFU data could add valuable insights into these scenarios.

5. Conclusion

In this work, we have presented the observations of the first candidate high-mass YSO close to Sgr A* using a data baseline of almost 30 yr with about four different telescopes in various wavelength regimes. In the following, we will outline our key findings and the related interpretation as discussed above.

1. In the NIR/MIR, we have identified several components related to the X3 system in the *H*, *K*, *L*, and *M* bands.
2. Because of the broad wavelength coverage, a coreless gas/dust feature can be excluded.
3. Based on the extensive data baseline covering two decades of observations, the components of the system (X3, X3a, X3b, X3c) move with a comparable proper motion toward the IRS 13 cluster.
4. The *H*- and *K*-band detection of X3a between 1995 and 2020 imply a stellar classification of this component of the X3 system. It is therefore plausible to classify X3a as the embedded stellar source of the dusty envelope X3.
5. Due to the missing NIR CO absorption lines and the depth of the $2.36 \mu\text{m}$ spectral feature, X3a is consistent with a young (proto)star rather than an evolved, late-type star.
6. The hot blob X3b with a decreasing distance toward the central stellar source X3a is below the detection limit in 2012 with no traceable emission in the following epochs. The independently calculated theoretical Hill radius matches the NIR observations and implies that X3b was likely accreted in 2011/2012.
7. For the hot *L*-band blob X3c, we find a constant distance toward X3a which suggests that it is created due to the thermal pressure of the ambient medium.
8. The spectroscopic footprint reveals a rich abundance of NIR emission lines.
9. We detect the P Cygni profile of the He I line, which indicates the presence of a wind with over -400 km s^{-1} terminal velocity. Such a high wind velocity is a common property of young stars.
10. A detailed analysis of the Br γ line reveals a continuous velocity gradient that coincides with the position of X3a implying a physical connection. This emission line is most likely connected to photoionized outflows/winds that might originate close to the protostar or a gaseous accretion disk.
11. This interpretation of the Br γ emission correlates with the MIR lines that originate in a dense and compact region.
12. The spatial distribution and dimensions of the NIR and MIR emission matches the size of the radio/submillimeter observations of the ionized H30 α line, implying that the ionization process might be produced by the same mechanism, namely, photoionized outflows.
13. The H30 α line is arranged in a ring-like structure with a diameter of about 2000 au and most likely shielded in an optically thick envelope in agreement with recent independent observations of massive YSOs, i.e., G28.200.05.
14. In general, the organic and complex molecules observed in the NIR and MIR are associated tracers for the presence of a YSO.

15. Based on our 3D MCMC radiative transfer calculations, we infer the stellar mass of $15_{-5}^{+10} M_{\odot}$ and an age of a few 10^4 yr for the X3 system,
16. Considering the 3D distance and proper motion of the X3 system, it may have been a former member of the IRS 13 cluster.

In terms of future perspective, we expect more insights into the X3 system with ERIS (VLT), MIRI (JWST), GRAVITY (VLTI), and METIS (ELT).

We thank the anonymous referee for the quick and constructive comments that helped to improve this paper. This work was supported in part by the Deutsche Forschungsgemeinschaft (DFG) via the Cologne Bonn Graduate School (BCGS), the Max Planck Society through the International Max Planck Research School (IMPRS) for Astronomy and Astrophysics as well as special funds through the University of Cologne. We acknowledge support for the Article Processing Charge from the DFG (German Research Foundation, 491454339). Conditions and Impact of Star Formation is carried out within the Collaborative Research Centre 956, subproject [A02], funded by the Deutsche Forschungsgemeinschaft (DFG) - project ID 184018867. M.Z. acknowledges the financial support by the National Science Center, Poland, grant No. 2017/26/A/ST9/00756 (Maestro 9) and NAWA financial support under the agreement PPN/WYM/2019/1/00064 to perform a three-month exchange stay at the Charles University in Prague and the Astronomical Institute of the Czech Academy of Sciences. M.Z. also acknowledges GAČR EXPRO grant 21-13491X (“Exploring the Hot Universe and Understanding Cosmic Feedback”) for financial support. Part of this work was supported by fruitful discussions with members of the European Union-funded COST Action MP0905: Black Holes in a Violent Universe and the Prague–Cologne Exchange Program for university students. V.K. thanks the Czech Science Foundation (No. 21-11268S). A.P., J.C., S.E., and G.B. contributed useful points to the discussion. We also would like to thank the members of the SINFONI/NACO/VISIR and ESO’s Paranal/Chile team for their support and collaboration.

This research has made use of the Keck Observatory Archive (KOA), which is operated by the W. M. Keck Observatory and the NASA Exoplanet Science Institute (NExScI), under contract with the National Aeronautics and Space Administration.

Facilities: HST (NICMOS), VLT (SINFONI, VISIR, ISAAC, and NACO), ALMA, KECK (NIRCAM2).

Software: astropy (Astropy Collaboration et al. 2013, 2018), Hyperion (Robitaille 2011), DPuser (Ott 2013).

Appendix

This appendix provides additional detections of the X3 system and lists the data used in this work. In addition, we present a preliminary Keplerian solution for the orbit of the X3 system.

Appendix A Data

Most of the data used in this work are freely available from the ESO, ALMA, and Keck archives and have already been analyzed in several related publications, such as

Table 7
H-band Data Observed with NACO between 2002 and 2019

NACO H Band		
Date	Observation ID	Number of Exposures
2002.08.30	60.A-9026(A)	25
2004.03.29	072.B-0285(B)	92
2006.10.15	078.B-0136(A)	48
2007.04.04	179.B-0261(A)	192
2007.07.21	179.B-0261(D)	192
2010.05.09	183.B-0100(T)	21
2012.07.21	088.B-0308(B)	28
2018.07.14	0101.B-0570(A)	29
2019.05.03	5102.B-0086(D)	29

Table 8
K-band Data Observed with NACO between 2002 and 2018

NACO K Band		
Date	Observation ID	Number of Exposures
2002.07.31	60.A-9026(A)	61
2003.06.13	713-0078(A)	253
2004.07.06	073.B-0775(A)	344
2004.07.08	073.B-0775(A)	285
2005.07.25	271.B-5019(A)	330
2005.07.27	075.B-0093(C)	158
2005.07.29	075.B-0093(C)	101
2005.07.30	075.B-0093(C)	187
2005.07.30	075.B-0093(C)	266
2005.08.02	075.B-0093(C)	80
2006.08.02	077.B-0014(D)	48
2006.09.23	077.B-0014(F)	48
2006.09.24	077.B-0014(F)	53
2006.10.03	077.B-0014(F)	48
2006.10.20	078.B-0136(A)	47
2007.03.04	078.B-0136(B)	48
2007.03.20	078.B-0136(B)	96
2007.04.04	179.B-0261(A)	63
2007.05.15	079.B-0018(A)	116
2008.02.23	179.B-0261(L)	72
2008.03.13	179.B-0261(L)	96
2008.04.08	179.B-0261(M)	96
2009.04.21	178.B-0261(W)	96
2009.05.03	183.B-0100(G)	144
2009.05.16	183.B-0100(G)	78
2009.07.03	183.B-0100(D)	80
2009.07.04	183.B-0100(D)	80
2009.07.05	183.B-0100(D)	139
2009.07.05	183.B-0100(D)	224
2009.07.06	183.B-0100(D)	56
2009.07.06	183.B-0100(D)	104
2009.08.10	183.B-0100(I)	62
2009.08.12	183.B-0100(I)	101
2010.03.29	183.B-0100(L)	96
2010.05.09	183.B-0100(T)	12
2010.05.09	183.B-0100(T)	24
2010.06.12	183.B-0100(T)	24
2010.06.16	183.B-0100(U)	48
2011.05.27	087.B-0017(A)	305
2012.05.17	089.B-0145(A)	169
2013.06.28	091.B-0183(A)	112
2017.06.16	598.B-0043(L)	36
2018.04.24	101.B-0052(B)	120

Table 9
L-band Data Observed with NACO between 2002 and 2018

NACO L Band		
Date	Observation ID	Number of Exposures
2002.08.30	060.A-9026(A)	80
2003.05.10	071.B-0077(A)	56
2004.07.06	073.B-0775(A)	217
2005.05.13	073.B-0085(E)	108
2005.06.20	073.B-0085(F)	100
2006.05.28	077.B-0552(A)	46
2006.06.01	077.B-0552(A)	244
2007.03.17	078.B-0136(B)	78
2007.04.01	179.B-0261(A)	96
2007.04.02	179.B-0261(A)	150
2007.04.02	179.B-0261(A)	72
2007.04.06	179.B-0261(A)	175
2007.06.09	179.B-0261(H)	40
2008.05.28	081.B-0648(A)	58
2008.08.05	179.B-0261(N)	64
2008.09.14	179.B-0261(U)	49
2009.03.29	179.B-0261(X)	32
2009.03.31	179.B-0261(X)	32
2009.04.03	082.B-0952(A)	42
2009.04.05	082.B-0952(A)	12
2009.09.19	183.B-0100(J)	132
2009.09.20	183.B-0100(J)	80
2010.07.02	183.B-0100(Q)	485
2011.05.25	087.B-0017(A)	29
2012.05.16	089.B-0145(A)	30
2013.05.09	091.C-0159(A)	30
2015.09.21	594.B-0498(G)	420
2016.03.23	096.B-0174(A)	60
2017.03.23	098.B-0214(B)	30
2018.04.22	0101.B-0065(A)	68
2018.04.24	0101.B-0065(A)	50

Table 10
M-band Data Observed with NACO in 2012

Date	Observation ID	Exp. Time	Band	Instrument/ Telescope
(YYYY: MM:DD)		(s)		
2012:03:17	088.B-1038(A)	2780	<i>M</i>	NACO/VLT

Table 11
VISIR MIR Data Covering the *N* and *Q* Bands Carried out in 2004

Date	Observation ID	Exp. Time	Filter/ Band	Instrument/ Telescope
(YYYY: MM:DD)		(s)		
2004:05:09	60.A-9234(A)	35	PAHr1	VISIR/VLT
2004:05:08	60.A-9234(A)	32	PAH	VISIR/VLT
2004:05:09	60.A-9234(A)	130	Ar III	VISIR/VLT
2004:05:09	60.A-9234(A)	12	SIVr1	VISIR/VLT
2004:05:09	60.A-9234(A)	30	SIVr2	VISIR/VLT
2004:05:07	60.A-9234(A)	950	PAH2	VISIR/VLT
2004:05:09	60.A-9234(A)	35	NeIIr1	VISIR/VLT
2004:05:08	60.A-9234(A)	171	Ne II	VISIR/VLT
2004:05:09	60.A-9234(A)	104	NeIIr2	VISIR/VLT
2004:05:09	60.A-9234(A)	62	Q2	VISIR/VLT
2004:05:09	60.A-9234(A)	340	Q3	VISIR/VLT

Table 12
ISAAC Data Observed in 2003 (Moultaka et al. 2005, 2015). The SL filter corresponds to 2.55–4.2 μm (LWS3)

Date	Observation ID	Exp. Time	Band	Instrument/ Telescope
(YYYY: MM:DD)		(s)		
2003:07:11	71.C-0192(A)	266	SL	ISAAC/VLT

Table 13
SINFONI Data Used for the Spectroscopic Analysis in This Work

Date	Observation ID	Exp. Time	Band	Instrument/ Telescope
(YYYY: MM:DD)		(s)		
2014.08.30	093.B-0218(B)	2700	<i>H+K</i>	SINFONI/VLT

Note. The final mosaic is created from nine single data cubes with an exposure time of 300 s each. AO is enabled for every observation.

Table 14
Keck Data Observed with NIRCAM2 and OSIRIS

Date	Observation ID	Exp. Time	Band	Instrument/ Telescope
(YYYY: MM:DD)		(s)		
2019.08.14	K311	1110	L	NIRCAM2/Keck
2019.08.14	K311	952	K	NIRCAM2/Keck
2019.08.14	K311	89	H	NIRCAM2/Keck
2020.08.03	E337	59	K	OSIRIS/Keck

Note. The L-band data are a combination of 37 single observations with an exposure time of 30 s each. The K-band data observed with NIRCAM2 consist of 34 single observations and an exposure time of 28 s each. The observations in 2020 were carried out with the OSIRIS science cam. For the stacked final mosaic, we used four single observations with an exposure time of 14.7 s each. The three single H-band observations exhibit an exposure time of about 30 s each.

Table 15
ALMA Data used in This Work

Date	Observation ID	Exp. Time	Band	Instrument/ Telescope
(YYYY: MM:DD)		(s)		
2016:08:30	2015.1.01080.S	11250	7 (CO)	ALMA
2017:05:09	2015.1.01080.S	27155	5 (H30 α)	ALMA

Note. The CO data were previously analyzed in, e.g., Tsuboi et al. (2017).

Witzel et al. (2012), Shahzamanian et al. (2016) and Peißker et al. (2020c, 2020d, 2020b, 2021a, 2021b, 2021c). For the H-band data, please consult Table 7. The K-, L-, and M-band data are listed in Tables 8, 9, and 10, respectively. In Tables 11 and 12, we index VISIR data from 2004 and ISAAC observations of 2003. The SINFONI IFU data of 2014 is listed in Table 13. For the multi-wavelength observations

carried out with the KECK observatory, examine Table 14. ALMA observations observed at 232 GHz and 343 GHz can be found in Table 15.

Appendix B **Multiwavelength Detection of X3**

In this section, we present the multiwavelength evolution of the X3 system covering almost two decades of NIR and MIR observations in the GC. This rich data set allows us to determine the properties of the X3 system. Although the *H*-band suffers from increased background noise (Figure 19), we find, in agreement with the *K*-band data, two objects (X3a and X3b) at the position of the green dashed circle (see Figure 20).

This green circle also represents the rough position of the dusty *L*-band envelope shown in Figure 21. Based on the proper-motion analysis shown in Figure 4, we find that the components move along toward the northwest (for the projected direction, see also Figure 11). In the *H* and *K* bands, we find two emission blobs that we denote as X3a and X3b. Although X3a can be observed throughout the data, X3b seems to fade out between 2002 and 2011. We also noticed a decreasing distance between the two sources. We note that X3b was brighter in 2002 compared to X3a. In addition to the NACO data presented, we use MIR narrow-line VISIR filters to investigate the X3 system for complex molecules (see Figure 22). As is expected for a YSO, we find prominent

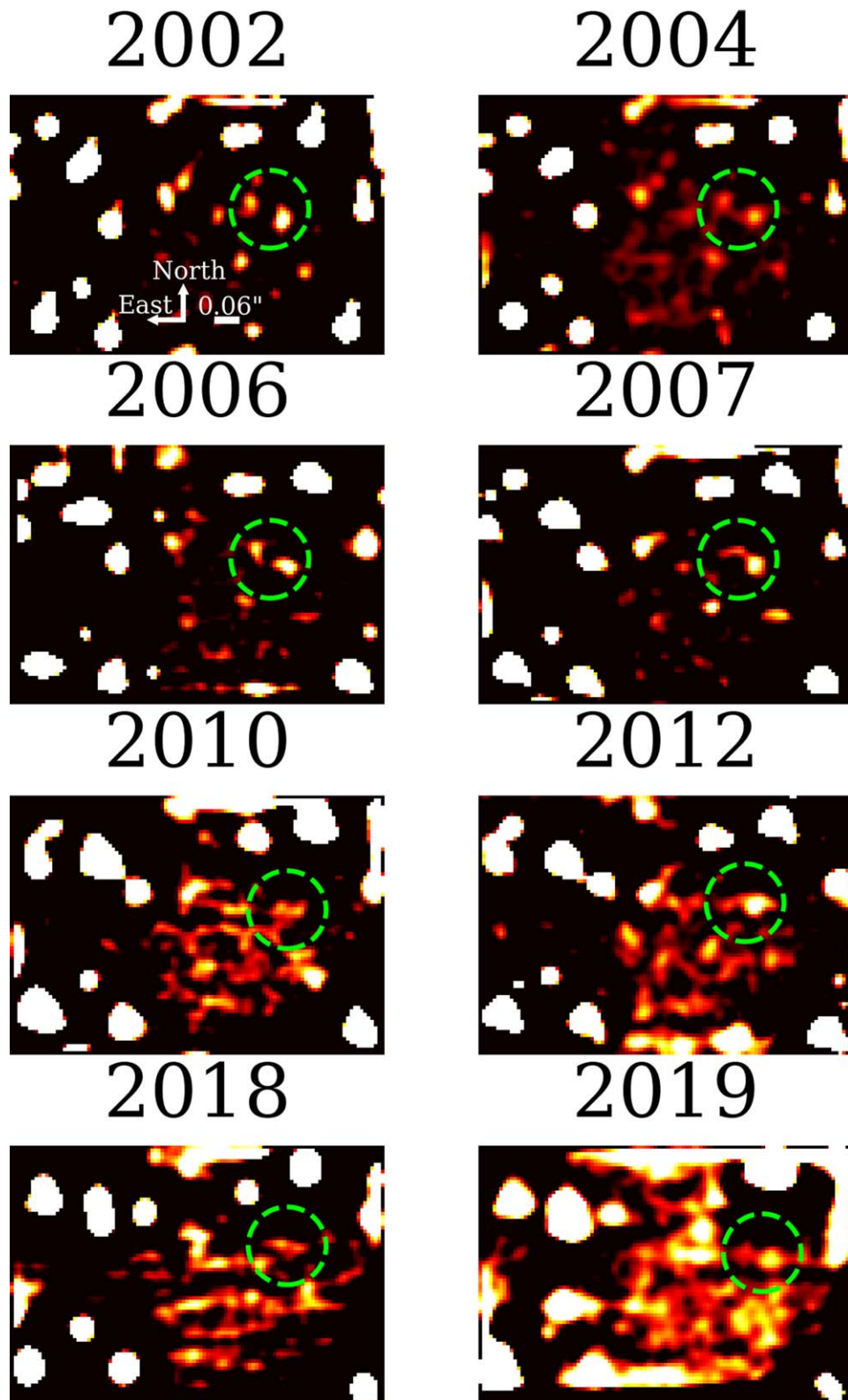


Figure 19. Observation of the X3 system in the H band with NACO (VLT) and NIRC2 (KECK) between 2002 and 2019. We indicate the position of X3a with a lime-colored dashed circle. Until 2010, we observe X3b, which seems to coincide with X3a in 2012. After 2012, X3b is below the detection limit. In contrast, X3a can be detected throughout the available data at the expected position.

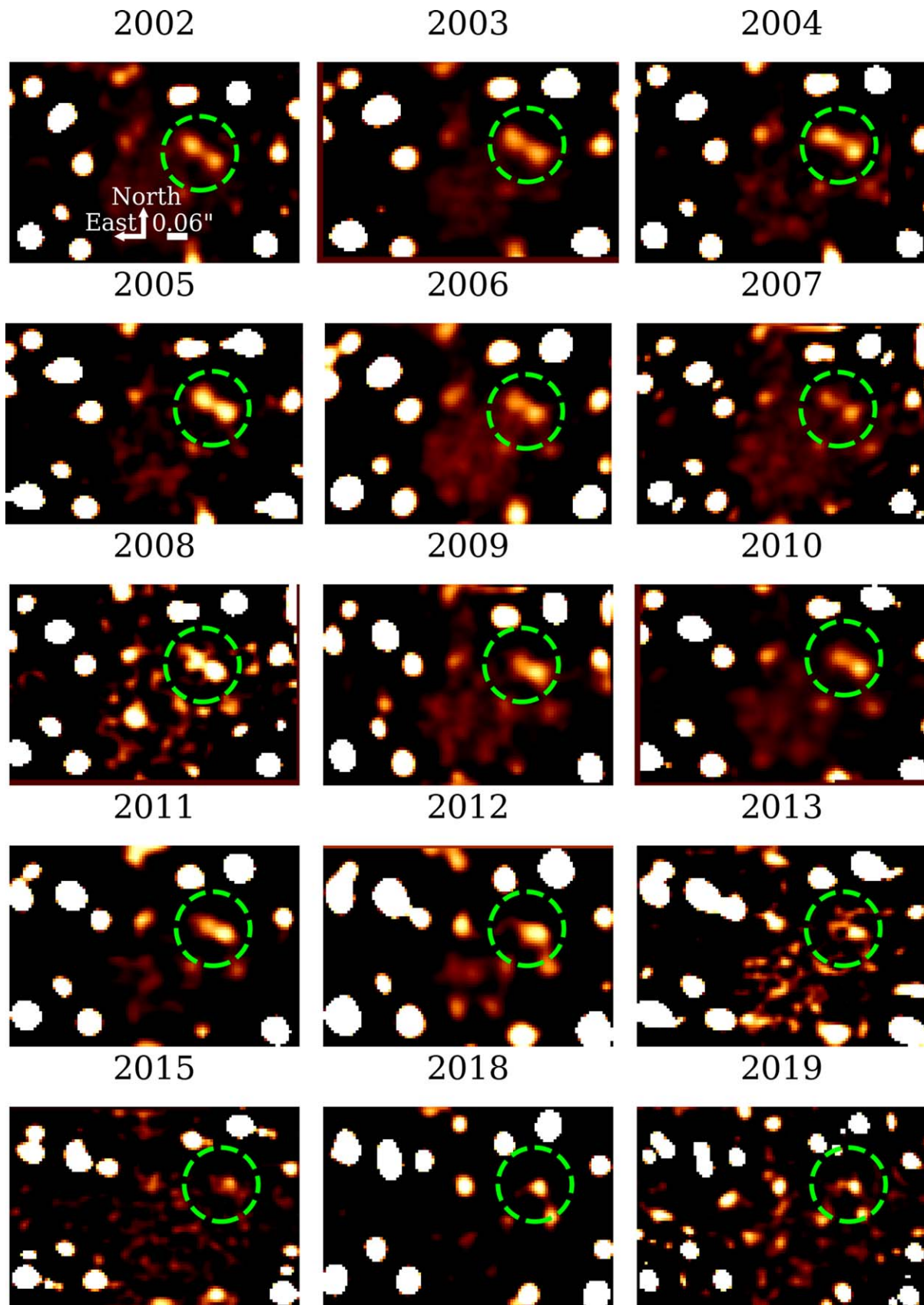


Figure 20. Observation of the X3 system in the K band with NACO (VLT) and NIRC2 (KECK) between 2002 and 2019. The data between 2002 and 2018 was observed with NACO, the data in 2019 with NIRC2. We indicate the position of X3a and X3b with a lime-colored dashed circle. Likewise in the H band, we do not find any emission above the noise for X3b after 2012. For a continuum observation of X3a in 2020, please see Figure 23.

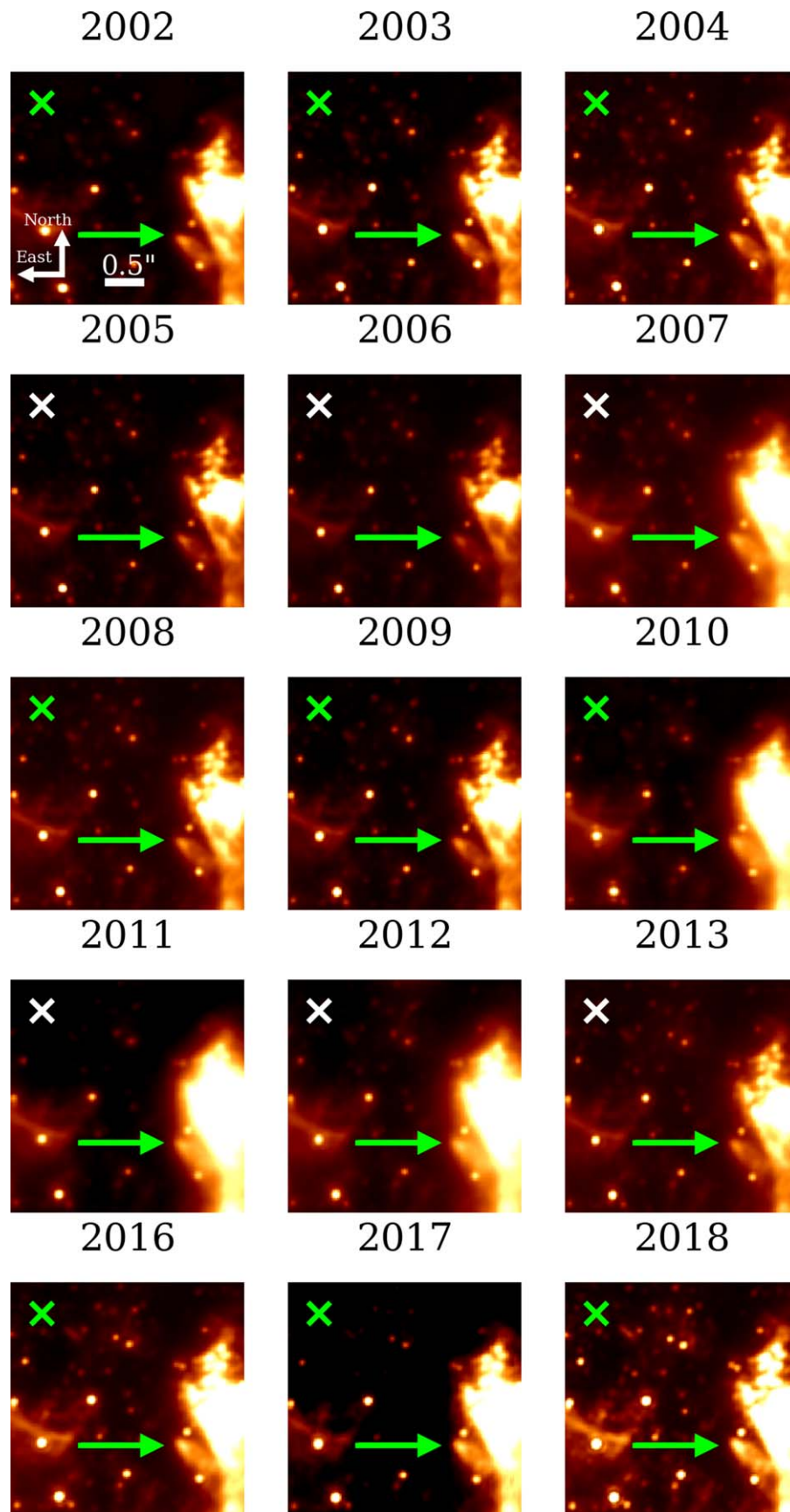


Figure 21. Observation of the X3 system in the L band with NACO between 2002 and 2018. The position of \times indicates the position of Sgr A * . The lime-colored arrow is pointing to the position of the bow shock X3.

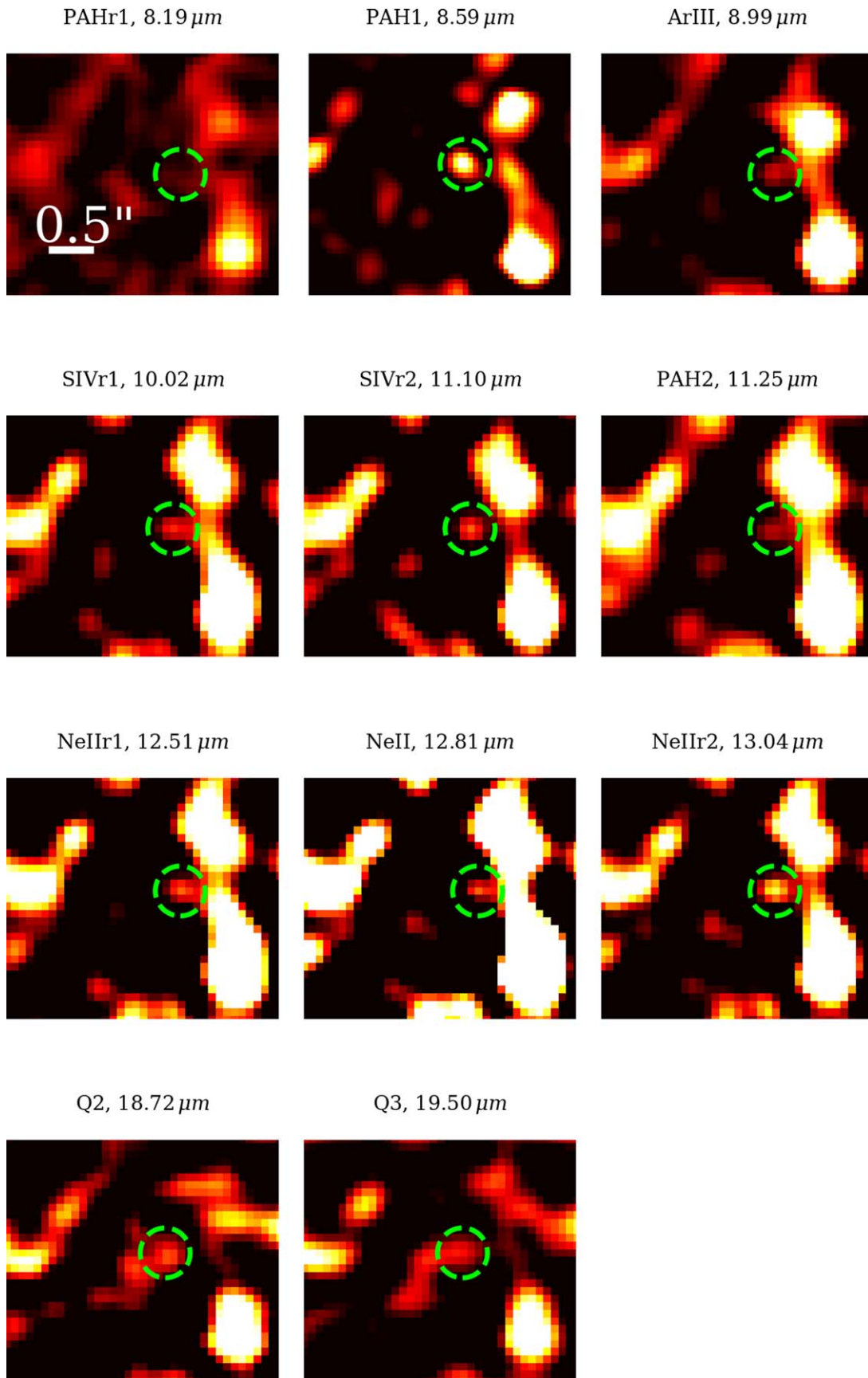


Figure 22. Observation of the X3 system with VISIR of 2004. The titles of these subpanels refer to the corresponding filters of VISIR. Every (complex) observed molecule originates in a compact region indicated by a lime-colored dashed circle. In every box, north is up and east is to the left.

Table 16
Orbital Elements of X3 using *L*-band NACO Data between 2002 and 2018

ID	a (mas)	e	i (°)	ω (°)	Ω (°)	t_{peri} (YT)
X3	440.26 ± 50	0.708 ± 0.21	78.49 ± 7.9	16.32 ± 9.3	226.31 ± 6.7	2090.05

emission lines in the MIR that originate within a compact area (Berrilli et al. 1992; Hartmann et al. 1993; Brooke et al. 1993).

Appendix C

The Keplerian Orbit of the X3 System

Due to the bright emission of X3 in the *L*-band in combination with the long data baseline, we investigated its evolution to derive a Keplerian solution of the orbit. We are aware of the challenges due to the elongated shape of X3. A more sophisticated approach should incorporate all bands in combination with a precise measurement of the LOS velocity of X3a to reduce the uncertainties. Currently, the Keplerian orbit can be treated as a quantitative approach. A more qualitative treatment of the orbit will be subject to future publications using 3D IFU data of MIRI/JWST. The resulting orbital elements of the *L*-band analysis are listed in Table 16.

Appendix D

Further Detections of the X3 System

In this section, we will show additional detections of the X3 system that support the analysis in this work. In Figure 23, we present data observed with the OH-Suppressing Infrared Imaging Spectrograph (OSIRIS) in 2020. The NIR instrument is mounted at the Keck telescope and works in a way comparable to that of SINFONI (VLT) with a slightly lower spatial pixel scale of 10 mas. We downloaded the reduced data from the Keck Online Archive and applied no further correction to the data. In agreement with the proper-motion analysis presented in this work, we find X3a at the expected position (blue dashed circle in Figure 23). In addition to the NIR detection with OSIRIS, we find the prominent MIR emission line $\text{P}\gamma$ (rest wavelength @ $3.7405 \mu\text{m}$) in the ISAAC data cube

OSIRIS (K-band), 2020

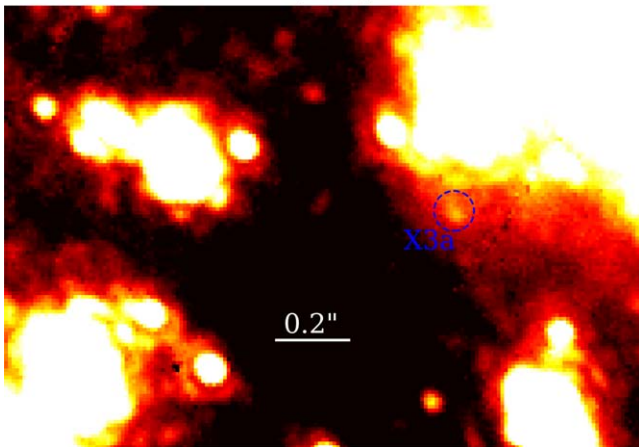


Figure 23. Continuum detection of X3a observed with OSIRIS in 2020. No filter is applied to the *K*-band data observed with KECK. Here, the dominant emission of the close-by cluster IRS 13 but also the nearby stars is eminent. The PSF wings of S3-374 are especially suppressing the emission of X3a, which motivates the use of a high-pass filter. The compact emission of X3a is located at the expected position based on the proper motion derived in this work (Figure 4). Consistent with the NACO *K*-band data, we derive a magnitude of $\text{mag}_{K\text{-band}} = 16.0_{-0.3}^{+0.7}$ mag.

$\text{P}\gamma$, *L*-band, ISAAC

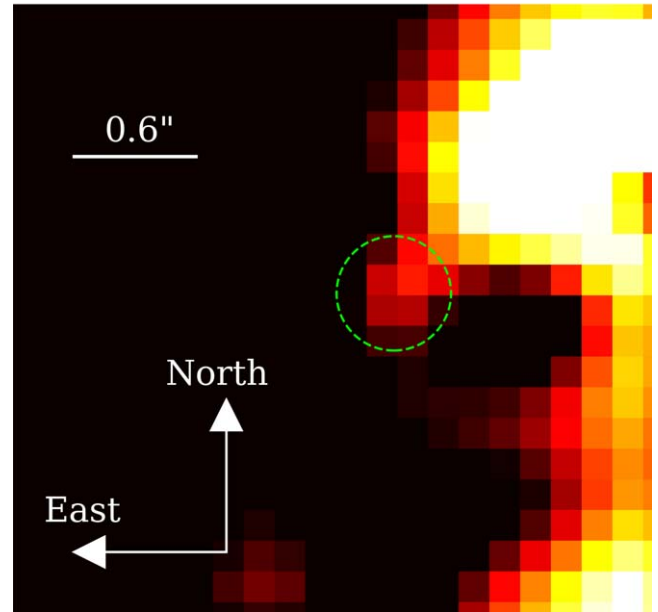


Figure 24. Combined continuum and $\text{P}\gamma$ line emission observed with ISAAC. The background-subtracted line map exhibits the X3 system (green dashed circle) close to the bright IRS 13 cluster. The used ISAAC data cube was previously analyzed in Moultaqa et al. (2005, 2015).

that is analyzed in Moultaqa et al. (2005). In Figure 24, we show a channel map of the related line. Due to the spatial and spectral resolution of the ISAAC data, the detection suffers from increased noise and artifacts. However, we find well above the confusion limit an indisputable emission of the X3 system suggesting the presence of hot dust, which is related to the envelope. The detection of a $\text{P}\gamma$ line is in agreement with the analysis of protoplanetary disks around YSOs (McClure et al. 2020).

Appendix E

Spectral Analysis of the X3 System

For the spectrum shown in Figure 7, we did not apply a background subtraction. While this might be a reasonable approach for many objects and sources outside the GC, we have shown in Valencia et al. (2015) the contamination that emerges from a variable background. In Figures 25 and 26, we show the same source spectrum as in Figure 7 but with nearby background subtraction. Due to the limitation of the FOV of $3''.2 \times 3''.2$ and the nearby IRS 13 cluster (see Figures 1 and 8), we limit the selection to a northern region around $1''.5$ away from X3a. We also inspect the impact of the background measured about $0''.55$ south of the source. As it is evident from both spectra, the overall detection of all features and lines is maintained. This is not completely unexpected since we investigate Doppler-shifted emission lines that are rather unique due to the limited FOV. In Peißker et al. (2021c), we have shown that SINFONI data observed in the GC might suffer from increased background noise. However, the isolation of Doppler-shifted lines and the related channel maps remains unquestionable and are reliable tools to

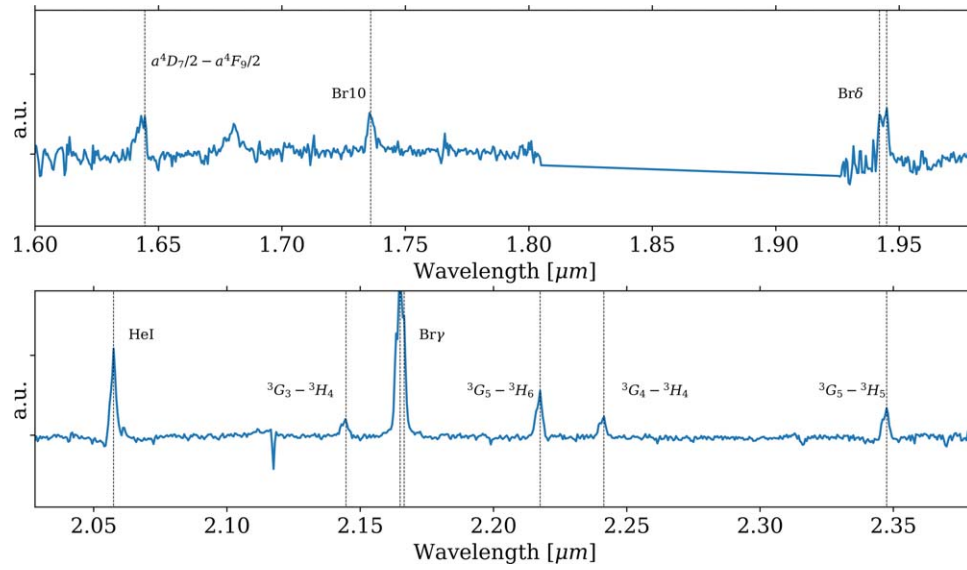


Figure 25. Near-infrared spectrum of X3a. We use a PSF-sized aperture and subtract a background that is located $1''.5$ north of X3a.

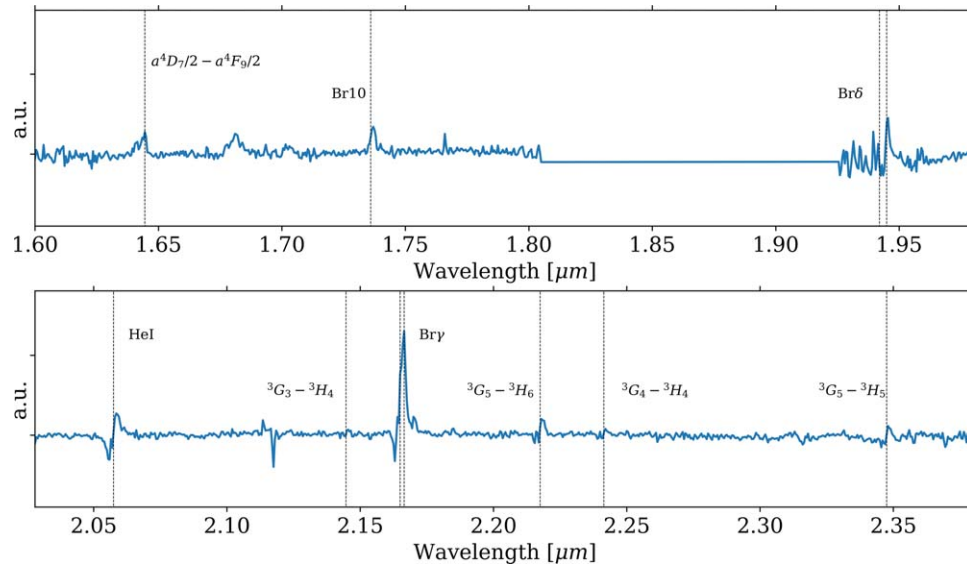


Figure 26. Same figure as Figure 25 but with a background that is located $0''.55$ south of X3a.

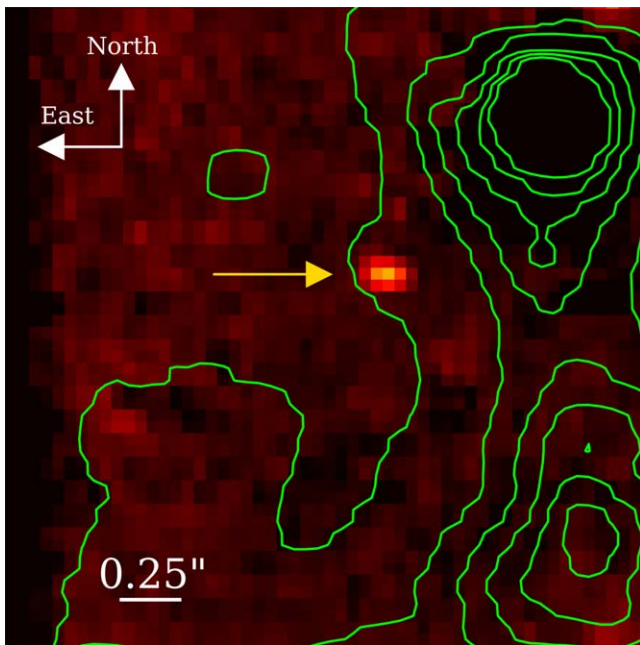


Figure 27. Line map of the H_2 emission line observed with SINFONI in 2014. The same FOV is shown in Figure 8, the lime-colored contour lines are adapted from the same figure showing the continuum emission of the environment of the X3 system. With a golden arrow, we indicate the position of X3a and the H_2 emission.

exhibit a physical connection between the investigated object and its spectrum. We demonstrate this relation by creating a line map for the Doppler-shifted H_2 line as presented in Figure 14. We integrate over the FWHM of the hydrogen line and subtract the closest channels that define the background. For a better comparison, we incorporate the contours from Figure 8, left plot. The resulting line map is shown in Figure 27, which marks an unambiguous detection of the Doppler-shifted H_2 line.

Appendix F

Spectral Energy Distribution of the S-cluster Star S2

Due to the lack of a flux density analysis of the S-cluster star S2 (Eckart & Genzel 1996; Parsa et al. 2017;

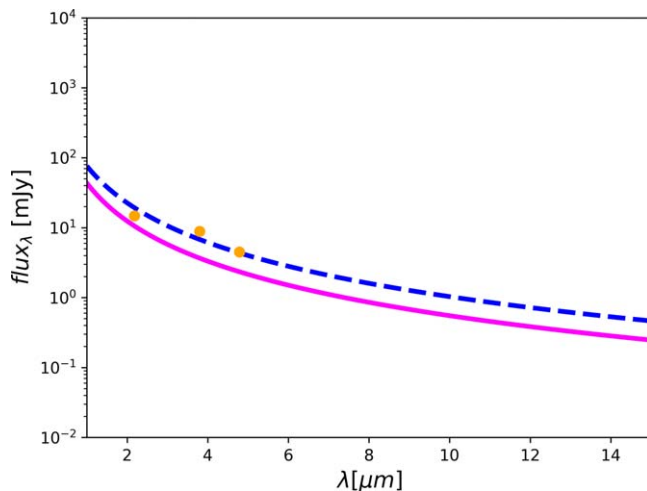


Figure 28. SED of the B2V star S2 based on a single-temperature blackbody fit. With this fit represented with a blue dashed line, we estimate the H -band flux density of S2 that can be used as a zero-flux point for the photometric analysis. We use $T_{\text{eff}} = 22,500$ K and $R = 8.5R_{\odot}$. The magenta solid line represents $T_{\text{eff}} = 28,500$ K and $R = 5.5R_{\odot}$ adopted from Habibi et al. (2017).

Hosseini et al. 2020) in the H band, we implement literature values derived for the K (Sabha et al. 2012), L (Viehmann et al. 2006), and M bands (Viehmann et al. 2006), see Figure 28. We used a single-temperature blackbody fit to estimate the H -band flux of about 32.0 ± 0.2 mJy. Based on the spectral atlas of Hanson et al. (1996), we use common B2V star properties to reproduce the stellar energy distribution.

ORCID iDs

Florian Peißker <https://orcid.org/0000-0002-9850-2708>
 Michal Zajaček <https://orcid.org/0000-0001-6450-1187>
 Nadeen B. Sabha <https://orcid.org/0000-0001-7134-9005>
 Masato Tsuboi <https://orcid.org/0000-0001-8185-8954>
 Jihane Moultaqa <https://orcid.org/0000-0001-9069-4955>
 Lucas Labadie <https://orcid.org/0000-0001-5342-5713>
 Andreas Eckart <https://orcid.org/0000-0001-6049-3132>
 Vladimír Karas <https://orcid.org/0000-0002-5760-0459>
 Lukas Steiniger <https://orcid.org/0000-0002-5859-3932>
 Matthias Subroweit <https://orcid.org/0000-0001-6165-8525>
 Anjana Suresh <https://orcid.org/0000-0001-7114-2389>
 Maria Melamed <https://orcid.org/0000-0002-4902-3794>
 Yann Clénet <https://orcid.org/0000-0002-8382-2020>

References

- Akiyama, K., Alberdi, A., Alef, W., et al. 2022, *ApJL*, 930, L12
 Alcalá, J. M., Natta, A., Manara, C. F., et al. 2014, *A&A*, 561, A2
 Ali, B., Paul, D., Eckart, A., et al. 2020, *ApJ*, 896, 100
 Astropy Collaboration, Price-Whelan, A. M., Sipőcz, B. M., et al. 2018, *AJ*, 156, 123
 Astropy Collaboration, Robitaille, T. P., Tollerud, E. J., et al. 2013, *A&A*, 558, A33
 Baganoff, F. K., Maeda, Y., Morris, M., et al. 2003, *ApJ*, 591, 891
 Barvainis, R. 1987, *ApJ*, 320, 537
 Beck, T. L., & Bary, J. S. 2019, *ApJ*, 884, 159
 Beck, T. L., Bary, J. S., & McGregor, P. J. 2010, *ApJ*, 722, 1360
 Berrilli, F., Corciulo, G., Ingrassio, G., et al. 1992, *ApJ*, 398, 254
 Bhat, H. K., Sabha, N. B., Zajaček, M., et al. 2022, *ApJ*, 929, 178
 Bonnell, I. A., & Rice, W. K. M. 2008, *Sci*, 321, 1060
 Bonnet, H., Abuter, R., Baker, A., et al. 2004, *Msngr*, 117, 17
 Bressan, A., Marigo, P., Girardi, L., et al. 2012, *MNRAS*, 427, 127
 Brooke, T. Y., Tokunaga, A. T., & Strom, S. E. 1993, *AJ*, 106, 656
 Buchholz, R. M., Schödel, R., & Eckart, A. 2009, *A&A*, 499, 483
 Christie, I. M., Petropoulou, M., Mimica, P., & Giannios, D. 2016, *MNRAS*, 459, 2420
 Ciurlo, A., Campbell, R. D., Morris, M. R., et al. 2020, *Natur*, 577, 337
 Clénet, Y., Rouan, D., Gratadour, D., Gendron, E., & Lacombe, F. 2003, in SF2A-2003: Semaine de l'Astrophysique Française, ed. F. Combes et al. (Les Ulis: EdP-Sciences), 163
 Cotera, A., Morris, M., Ghez, A. M., et al. 1999, in ASP Conf. Ser. 186, The Central Parsec of the Galaxy, ed. H. Falcke et al. (San Francisco, CA: ASP), 240
 Davies, R., Esposito, S., Schmid, H. M., et al. 2018, *Proc. SPIE*, 10702, 1070209
 Davis, C. J., Cervantes, B., Nisini, B., et al. 2011, *A&A*, 528, A3
 Do, T., Hees, A., Ghez, A., et al. 2019, *Sci*, 365, 664
 Draine, B. T. 2003, *ARA&A*, 41, 241
 Eckart, A., & Genzel, R. 1996, *Natur*, 383, 415
 Eckart, A., Moultaqa, J., Viehmann, T., Straubmeier, C., & Mouawad, N. 2004, *ApJ*, 602, 760
 Eckart, A., Mužić, A., Yazici, A., et al. 2013, *A&A*, 551, A18
 Eisenhauer, F., Abuter, R., Bickert, K., et al. 2003, *Proc. SPIE*, 4841, 1548
 Fritz, T. K., Gillessen, S., Dodds-Eden, K., et al. 2011, *ApJ*, 737, 73
 Frost, A. J., Oudmaijer, R. D., de Wit, W. J., & Lumsden, S. L. 2019, *A&A*, 625, A44
 Gallego-Cano, E., Schödel, R., Dong, H., et al. 2018, *A&A*, 609, A26
 Gardner, C. L., Jones, J. R., & Hodapp, K. W. 2016, *ApJ*, 830, 113
 Gautam, A. K., Do, T., Ghez, A. M., et al. 2019, *ApJ*, 871, 103
 Genzel, R., Eisenhauer, F., & Gillessen, S. 2010, *RvMP*, 82, 3121

- Genzel, R., Pichon, C., Eckart, A., Gerhard, O. E., & Ott, T. 2000, *MNRAS*, **317**, 348
- Glassgold, A. E., Najita, J., & Igea, J. 2004, *ApJ*, **615**, 972
- GRAVITY Collaboration, Bouvarour, Y. I., Perraut, K., et al. 2020, *A&A*, **642**, A162
- GRAVITY Collaboration, Wojtczak, J. A., Labadie, L., et al. 2023, *A&A*, **669**, A59
- Green, S., Mackey, J., Kavanagh, P., et al. 2022, *A&A*, **665**, A35
- Habibi, M., Gillessen, S., Martins, F., et al. 2017, *ApJ*, **847**, 120
- Hanson, M. M., Conti, P. S., & Rieke, M. J. 1996, *ApJS*, **107**, 281
- Hartmann, L., Kenyon, S. J., & Calvet, N. 1993, *ApJ*, **407**, 219
- Haworth, T. J., Clarke, C. J., & Owen, J. E. 2016, *MNRAS*, **457**, 1905
- Hobbs, A., & Nayakshin, S. 2009, *MNRAS*, **394**, 191
- Hosseini, S. E., Zajaček, M., Eckart, A., Sabha, N. B., & Labadie, L. 2020, *A&A*, **644**, A105
- Hsieh, P.-Y., Koch, P. M., Kim, W.-T., et al. 2021, *ApJ*, **913**, 94
- Jalali, B., Pelupessy, F. I., Eckart, A., et al. 2014, *MNRAS*, **444**, 1205
- Krabbe, A., Genzel, R., Drapatz, S., & Rotaciuc, V. 1991, *ApJL*, **382**, L19
- Krabbe, A., Genzel, R., Eckart, A., et al. 1995, *ApJL*, **447**, L95
- Kraus, S., Monnier, J. D., Che, X., et al. 2012, *ApJ*, **744**, 19
- Kumar, M. S. N., Bachiller, R., & Davis, C. J. 2002, *ApJ*, **576**, 313
- Lagage, P. O., Pel, J. W., Authier, M., et al. 2004, *Msngr*, **117**, 12
- Larkin, J., Barczys, M., Krabbe, A., et al. 2006, *Proc. SPIE*, **6269**, 62691A
- Larson, R. B. 1981, *MNRAS*, **194**, 809
- Law, C.-Y., Tan, J. C., Gorai, P., et al. 2022, *ApJ*, **939**, 120
- Lenzen, R., Hartung, M., Brandner, W., et al. 2003, *Proc. SPIE*, **4841**, 944
- Lu, J. R., Do, T., Ghez, A. M., et al. 2013, *ApJ*, **764**, 155
- Lucy, L. B. 1974, *AJ*, **79**, 745
- Maaskant, K. M., Min, M., Waters, L. B. F. M., & Tielens, A. G. G. M. 2014, *A&A*, **563**, A78
- Maillard, J. P., Paumard, T., Stolovy, S. R., & Rigaut, F. 2004, *A&A*, **423**, 155
- Marois, C., Lafrenière, D., Doyon, R., Macintosh, B., & Nadeau, D. 2006, *ApJ*, **641**, 556
- Matsuda, T., Isaka, H., & Ohsugi, Y. 2015, *PTEP*, **2015**, 113E01
- Maureira, M. J., Gong, M., Pineda, J. E., et al. 2022, *ApJL*, **941**, L23
- McClure, M. K., Dominik, C., & Kama, M. 2020, *A&A*, **642**, L15
- Menten, K. M., Reid, M. J., Eckart, A., & Genzel, R. 1997, *ApJL*, **475**, L111
- Mieda, E., Wright, S. A., Larkin, J. E., et al. 2014, *PASP*, **126**, 250
- Mizumoto, M., Kobayashi, N., Hamano, S., et al. 2018, *MNRAS*, **481**, 793
- Moorwood, A., Cuby, J. G., Biereichel, P., et al. 1998, *Msngr*, **94**, 7
- Morris, M. 1993, *ApJ*, **408**, 496
- Moser, L., Sánchez-Monge, Á., Eckart, A., et al. 2017, *A&A*, **603**, A68
- Moultaka, J., Eckart, A., & Mužić, K. 2015, *ApJ*, **806**, 202
- Moultaka, J., Eckart, A., Schödel, R., Viehmann, T., & Najarro, F. 2005, *A&A*, **443**, 163
- Murchikova, E. M., Phinney, E. S., Pancoast, A., & Blandford, R. D. 2019, *Natur*, **570**, 83
- Mužić, K., Eckart, A., Schödel, R., et al. 2010, *A&A*, **521**, A13
- Mužić, K., Schödel, R., Eckart, A., Meyer, L., & Zensus, A. 2008, *A&A*, **482**, 173
- Nayakshin, S., Cuadra, J., & Springel, V. 2007, *MNRAS*, **379**, 21
- Nisini, B., Milillo, A., Saraceno, P., & Vitali, F. 1995, *A&A*, **302**, 169
- Ott, T. 2013, DPUSER: Interactive Language for Image Analysis, Astrophysics Source Code Library, ascl:1303.025
- Ott, T., Eckart, A., & Genzel, R. 1999, *ApJ*, **523**, 248
- Owen, J. E., & Lin, D. N. C. 2023, *MNRAS*, **519**, 397
- Parsa, M., Eckart, A., Shahzamanian, B., et al. 2017, *ApJ*, **845**, 22
- Paumard, T., Genzel, R., Martins, F., et al. 2006, *ApJ*, **643**, 1011
- Peißker, F., Ali, B., Zajaček, M., et al. 2021a, *ApJ*, **909**, 62
- Peißker, F., Eckart, A., & Ali, B. 2021b, *ApJ*, **918**, 25
- Peißker, F., Eckart, A., & Parsa, M. 2020a, *ApJ*, **889**, 61
- Peißker, F., Eckart, A., Sabha, N. B., Zajaček, M., & Bhat, H. 2020c, *ApJ*, **897**, 28
- Peißker, F., Eckart, A., Zajaček, M., Ali, B., & Parsa, M. 2020d, *ApJ*, **899**, 50
- Peißker, F., Eckart, A., Zajaček, M., & Britzen, S. 2022, *ApJ*, **933**, 49
- Peißker, F., Hosseini, S. E., Zajaček, M., et al. 2020b, *A&A*, **634**, A35
- Peißker, F., Zajaček, M., Eckart, A., et al. 2019, *A&A*, **624**, A97
- Peißker, F., Zajaček, M., Eckart, A., et al. 2021c, *ApJ*, **923**, 69
- Plewa, P. M., Gillessen, S., Bauböck, M., et al. 2018, *RNAAS*, **2**, 35
- Portegies Zwart, S. F., McMillan, S. L. W., & Gerhard, O. 2003, *ApJ*, **593**, 352
- Pott, J. U., Eckart, A., Glindemann, A., et al. 2008, *A&A*, **480**, 115
- Schödel, R., Ratzka, T., Gehring, T., et al. 2011, *A&A*, **530**, A40
- Robitaille, T. P. 2011, *A&A*, **536**, A79
- Rousset, G., Lacombe, F., Puget, P., et al. 2003, *Proc. SPIE*, **4839**, 140
- Sabha, N., Eckart, A., Merritt, D., et al. 2012, *A&A*, **545**, A70
- Schödel, R., Najarro, F., Muzic, K., & Eckart, A. 2010, *A&A*, **511**, A18
- Scoville, N., & Burkert, A. 2013, *ApJ*, **768**, 108
- Shahzamanian, B., Eckart, A., Zajaček, M., et al. 2016, *A&A*, **593**, A131
- Sicilia-Aguilar, A., Banzatti, A., Carmona, A., et al. 2016, *PASA*, **33**, e059
- Tanaka, K. E. I., Tan, J. C., & Zhang, Y. 2016, *ApJ*, **818**, 52
- Tatulli, E., Isella, A., Natta, A., et al. 2007, *A&A*, **464**, 55
- Thi, W. F., van Dishoeck, E. F., Blake, G. A., et al. 2001, *ApJ*, **561**, 1074
- Tokunaga, A. T., & Vacca, W. D. 2007, in ASP Conf. Ser. 364, The Future of Photometric, Spectrophotometric and Polarimetric Standardization, ed. C. Sterken (San Francisco, CA: ASP), **409**
- Tsuboi, M., Kitamura, Y., Tsutsumi, T., et al. 2019, *PASJ*, **71**, 105
- Tsuboi, M., Kitamura, Y., Tsutsumi, T., et al. 2020a, *PASJ*, **72**, 36
- Tsuboi, M., Kitamura, Y., Tsutsumi, T., et al. 2020b, *PASJ*, **72**, L5
- Tsuboi, M., Kitamura, Y., Uehara, K., et al. 2017, *ApJ*, **842**, 94
- Ulrich, R. K. 1976, *ApJ*, **210**, 377
- Valencia, S. M., Eckart, A., Zajaček, M., et al. 2015, *ApJ*, **800**, 125
- Viehmann, T. 2007, PhD thesis, Andreas Eckart Univ. Cologne, Germany
- Viehmann, T., Eckart, A., Schödel, R., Pott, J. U., & Moultaka, J. 2006, *ApJ*, **642**, 861
- Ward, J. L., Oliveira, J. M., van Loon, J. T., & Sewilo, M. 2017, *MNRAS*, **464**, 1512
- Wardle, M., & Yusef-Zadeh, F. 1992, *Natur*, **357**, 308
- Whitney, B. A., Indebetouw, R., Bjorkman, J. E., & Wood, K. 2004, *ApJ*, **617**, 1177
- Wichittanakom, C., Oudmaijer, R. D., Fairlamb, J. R., et al. 2020, *MNRAS*, **493**, 234
- Wilkin, F. P. 1996, *ApJL*, **459**, L31
- Witzel, G., Eckart, A., Bremer, M., et al. 2012, *ApJS*, **203**, 18
- Woitke, P., Min, M., Thi, W. F., et al. 2018, *A&A*, **618**, A57
- Yusef-Zadeh, F., Roberts, D. A., Wardle, M., et al. 2015, *ApJL*, **801**, L26
- Yusef-Zadeh, F., Royster, M., Wardle, M., et al. 2013, *ApJL*, **767**, L32
- Yusef-Zadeh, F., Wardle, M., Kunneriath, D., et al. 2017, *ApJL*, **850**, L30
- Zajaček, M., Britzen, S., Eckart, A., et al. 2017, *A&A*, **602**, A121
- Zhu, Z., Li, Z., Ciurlo, A., et al. 2020, *ApJ*, **897**, 135